

Total Variation and Mean Curvature PDEs on the Homogeneous Space of Positions and Orientations

Bart Smets · Remco Duits · Etienne St-Onge · Jim Portegies

Received: date / Accepted: date

Abstract Two key ideas have greatly improved techniques for image enhancement and denoising: the lifting of image data to multi-orientation distributions (e.g. orientation scores), and the application of nonlinear PDEs such as Total Variation Flow (TVF) and Mean Curvature Flow (MCF). These two ideas were recently combined by Chambolle & Pock (for TVF) and Citti et al. (for MCF) for two-dimensional images.

In this work, we extend their approach to enhance and denoise images of arbitrary dimension, creating a unified geometric and algorithmic PDE framework, relying on (sub-)Riemannian geometry. In particular, we follow a different numerical approach, for which we prove convergence in the case of TVF by an application of Brezis-Komura gradient flow theory. Our framework also allows for additional data-adaptation through the use of locally adaptive frames and coherence enhancement techniques.

We apply TVF and MCF to the enhancement and denoising of elongated structures in 2D images via orientation scores, and compare the results to Perona-Malik diffusion and BM3D. We also demonstrate our techniques in 3D in the denoising and enhancement of crossing fiber bundles in DW-MRI. In comparison to data-driven diffusions, we see a better preservation of bundle boundaries and angular sharpness in fiber orientation densities at crossings.

Keywords Total Variation · Mean Curvature · Sub-Riemannian Geometry · Roto-Translations · Denoising · Fiber Enhancement

Bart Smets · Remco Duits · Jim Portegies
CASA, Eindhoven University of Technology
P.O. Box 513, 5600 MB Eindhoven, The Netherlands
E-mail: b.m.n.smets@tue.nl

Etienne St-Onge
SCIL, Sherbrooke Connectivity Imaging Lab, Canada

1 Introduction

In the last decade, many PDE-based image-analysis techniques for tracking and enhancement of curvilinear structures in images took advantage of lifting image data, typically defined on \mathbb{R}^d , to a multi-orientation distribution (e.g. an orientation score) defined on the homogeneous space $\mathbb{M}_d = \mathbb{R}^d \rtimes S^{d-1}$ of d -dimensional positions and orientations, see Fig. 1 and [7, 9, 11, 13, 17, 38]. After lifting the image to an orientation score, the score is taken as an initial condition of a PDE flow. After flowing the PDE for a short time, one obtains a regularized version of the original score, and by integration over all orientations, one obtains a regularized version of the original image.

The key advantage of lifting the images from \mathbb{R}^d to the homogeneous space \mathbb{M}_d is that the PDE flow can act differently on substructures with different orientations [7, 21, 11]. For instance, if the image contains two crossing lines, the PDE can regularize the two lines independently, rather than regularizing the whole crossing. Similarly, if the image contains a corner, the corner is preserved in the regularized image.

This idea of lifting images has been successfully implemented for image enhancement [12, 24], geodesic tracking [8, 11, 36], image denoising [2], contrast perception and optical illusions [3]. For instance, Perona-Malik diffusion has been lifted to the homogeneous space \mathbb{M}_d [15] and coherence enhancing diffusion (CED) [39] has been lifted to the method of *coherence enhancing diffusion on invertible orientation scores* (CED-OS) [24] and to its 3D generalization [27].

PDE-flows on orientation lifts of *3D images* ($d = 3$) are relevant for applications such as fiber enhancement [15, 38, 34, 18] and fiber tracking [33] in Diffusion-Weighted Magnetic Resonance Imaging (DW-MRI), and in enhancement [27] and tracking [14] of blood vessels in 3D images.

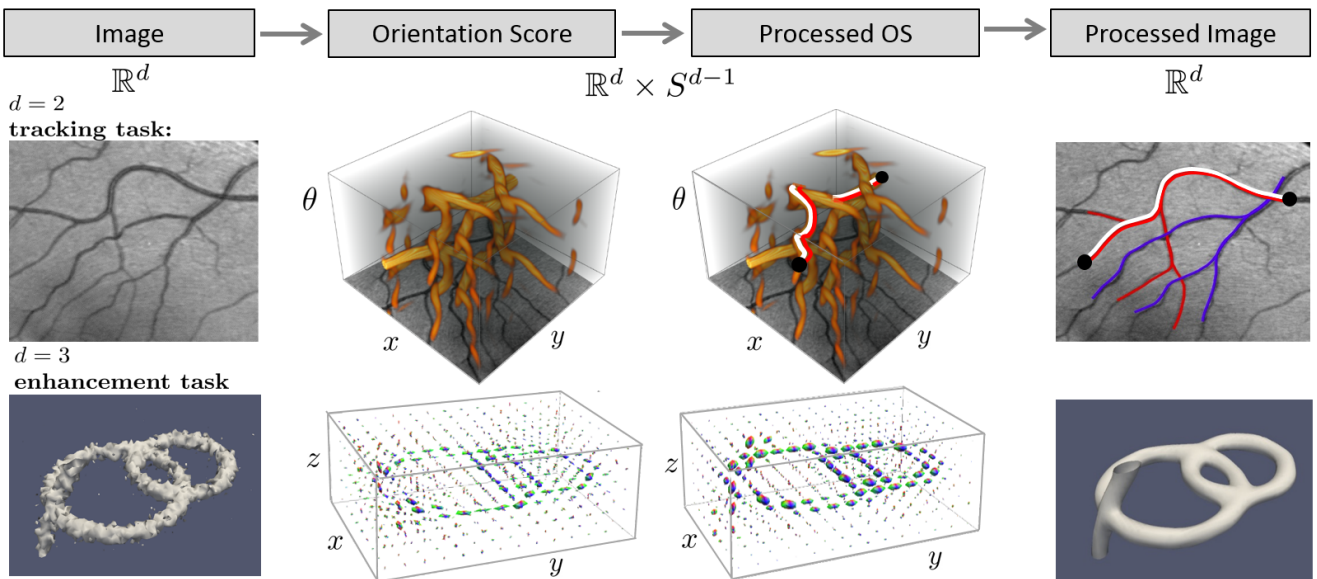


Fig. 1: Instead of direct PDE-based processing of an image, we apply PDE-based processing on a lifted image $U : \mathbb{R}^d \times S^{d-1} \rightarrow \mathbb{R}$ (e.g. an orientation score: OS). The OS is obtained by convolving the image with a set of rotated wavelets allowing for stable reconstruction [17, 7, 27]. 2nd row: Vessel-tracking in a 2D image via geodesic PDE-flows in OS that underly TVF: [7, 21, 11], with $\mathbf{n} = (\cos \theta, \sin \theta)^T \in S^1$. 3rd row: CED-OS diffusion of a 3D image [27, 20] visualized as a field of angular profiles (see remark 1). In this article we study image enhancement and denoising via TVF and MCF on $\mathbb{M}_d = \mathbb{R}^d \times S^{d-1}$ and compare to nonlinear diffusion methods.

The general workflow is illustrated in Fig. 1. The original image is encoded by a function $f : \Omega_f \rightarrow \mathbb{R}^+$, where $\Omega_f \subset \mathbb{R}^d$ is its support. From f , one computes an orientation lift $U \in C^1(\mathbb{M}_d, \mathbb{R})$, compactly supported within

$$\Omega = \Omega_f \times S^{d-1} \subset \mathbb{M}_d. \quad (1)$$

There are various ways to construct such a lift: it can be (the real part of) an invertible orientation score [19] (cf. Fig. 1), a channel-representation [23], a lift by Gabor wavelets [5], or a fiber orientation density [32], where in general the absolute value $|U(\mathbf{x}, \mathbf{n})|$ is a probability density of finding a fiber structure at position $\mathbf{x} \in \mathbb{R}^d$ with local orientation $\mathbf{n} \in S^{d-1}$. The orientation lift U is taken as an initial condition of a PDE flow $U \mapsto \Phi_t(U)$ with evolution time $t > 0$. Finally, the processed orientation score $\Phi_t(U)$ is integrated over all orientations to obtain the enhanced image f_t . In this article, we will work with the orientation score, with the main motivation being that this operation is invertible, so that at time $t = 0$, the output equals the input, i.e. $f_0 = f$.

The enhanced image that one obtains after running a PDE flow, (the bottom-right picture in Fig. 1), naturally depends on the type of flow used. One flow may be more suitable than another, depending on the requirements one puts on the resulting image. In case it is important to preserve sharp transitions in the image, nonlinear flows such as total variation flows (TVF) and mean curvature flow (MCF) are typically more suitable than nonlinear diffusion flows.

For $d = 2$, TVF and MCF were recently generalized to lifted images by Chambolle & Pock [11] and Citti et al. [12] respectively.

Their promising results have motivated us to generalize TVF and MCF to lifted images for general dimension d and provide a general geometric and algorithmic framework that can accommodate features such as locally adaptive frames and coherence enhancement.

The benefits of our approach are that we obtain a single unifying geometric and algorithmic framework for arbitrary d , with algorithms (for $d = 2, 3$) that preserve crossing lines, corners, plateaus, edges and bundle boundaries and can improve curvature adaptation via the optional inclusion of locally adaptive frames.

The structure of this article is as follows. We start by recapitulating orientation scores and explaining the homogeneous space \mathbb{M}_d as a Lie group quotient in the rigid body motion group $SE(d)$ in Section 2 and explain the necessary geometrical concepts. In Section 3, we introduce the PDEs for total variation and mean curvature flow on \mathbb{M}_d and introduce our explicit discretization scheme. Our numerical scheme includes regularization (to deal with a possible divide-by-zero) for which we prove convergence in Section 4. In Section 5 we evaluate the potential of our methods with 2D and 3D experiments.

Remark 1 (Visualization of 3D orientation scores).

In the 3rd row of Fig. 1, and henceforth, we visualize a lifted image $U : \mathbb{R}^3 \times S^2 \rightarrow \mathbb{R}^+$ by a grid of angular profiles $\{\mu U(\mathbf{x}, \mathbf{n}) \mid \mathbf{x} \in \mathbb{Z}^3, \mathbf{n} \in S^2\}$, with fixed $\mu > 0$.

Remark 2 (Additional content in this version).

In comparison to the original SSVM paper[1] this article adds the following:

- A more comprehensive treatment of the geometrical tools used such as vector fields and metric tensors. We make a clear distinction between the group $SE(d)$ and the homogeneous space \mathbb{M}_d and explain how the objects we use translate between the two.
- A coordinate free formulation of gauge frame fitting that agrees with the coordinate approach of [20].
- A general formulation of the coherence enhancement technique for TVF and MCF.
- A proof for the theorem of the strong convergence, stability and accuracy of TV-flows.
- Extended reporting on the 2D denoising/enhancing experiments we performed, including a comparison of isotropic vs. anisotropic processing and the effect of the inclusion of coherence enhancement in TVF and MCF.
- Additional comparison in 2D against Perona-Malik[30] diffusion and BM3D[42, 43].

2 Preliminary Theory

Before we can provide the generalized PDEs which include TVF and MCF as special cases we need to construct the necessary tools, to which we devote this section. Starting with a recapitulation of orientation scores.

2.1 Orientation Scores: Lifting the image domain from \mathbb{R}^d to \mathbb{M}_d

In order to disentangle all local orientations in an image we lift the data from position space \mathbb{R}^d to the homogeneous space \mathbb{M}_d of positions and orientations, This means that we extend the domain of an image. See Fig. 1, where we lift the data from \mathbb{R}^d towards \mathbb{M}_d via invertible orientation scores.

Building an orientation score starts with selecting an orientation-sensitive filter (or wavelet) $\psi \in L^1 \cap L^2(\mathbb{R}^d)$. We can then (under appropriate conditions[17, 27]) filter out a particular direction from an image $f \in L^2(\mathbb{R}^d)$ by convolving the image with this filter aligned to that direction. An orientation score $\mathcal{W}_\psi f$ can then be constructed by applying this filtering for all directions $\mathbf{n} \in S^{d-1}$:

$$\mathcal{W}_\psi f(\mathbf{x}, \mathbf{n}) = \int_{\mathbb{R}^d} \overline{\psi(\mathbf{R}_\mathbf{n}^{-1}(\mathbf{y} - \mathbf{x}))} f(\mathbf{y}) d\mathbf{y}, \quad (2)$$

for all $\mathbf{x} \in \mathbb{R}^d$ and rotations $\mathbf{R}_\mathbf{n}$ that map a reference axis $\mathbf{a} \in S^{d-1}$ to \mathbf{n} .

For this paper we will be using *cake wavelets* [17, 27] for our filter ψ , illustrated in Fig. 2 for $d = 2$. These wavelets are directional filters that have the property that we can accurately reconstruct the original image from the orientation score (again under appropriate conditions) by integration over S^{d-1} , i.e.

$$f(\mathbf{x}) \approx \int_{S^{d-1}} \mathcal{W}_\psi f(\mathbf{x}, \mathbf{n}) d\sigma(\mathbf{n}), \quad (3)$$

where σ denotes the usual surface measure over S^{d-1} . We always use standard cake wavelet parameter settings from [28] in our experiments.

The explicit formulas for these cake wavelets that allow invertible orientation scores are available in [7, 17] and specifically for $d = 3$ in [27]. An intuitive illustration of an orientation score can be seen in Fig. 2.

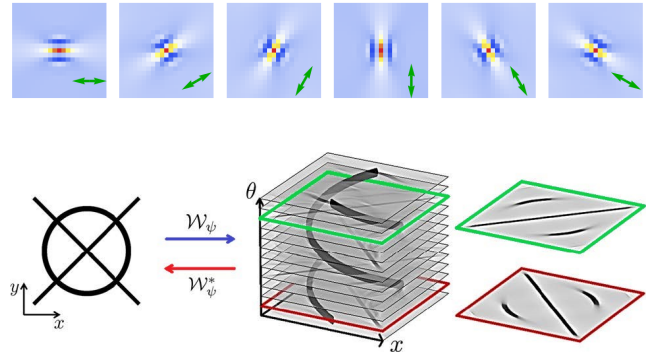


Fig. 2: Top: cake wavelets[17] for $d = 2$ used to directionally filter an image and construct an orientation score. Bottom: how orientation scores disentangle orientations.

2.2 $SE(d)$ and the Homogeneous Space of Positions and Orientations \mathbb{M}_d

Consider the rigid body motion group $SE(d) = \mathbb{R}^d \times SO(d)$, the semi-direct product of the translation group \mathbb{R}^d and the rotation group $SO(d)$ of orthogonal $d \times d$ matrices. We call elements of $SE(d)$ *roto-translations*. The product of two roto-translations $g_i = (\mathbf{x}_i, \mathbf{R}_i)$ in $SE(d)$ is given by

$$g_1 g_2 = (\mathbf{x}_1, \mathbf{R}_1) (\mathbf{x}_2, \mathbf{R}_2) := (\mathbf{x}_1 + \mathbf{R}_1 \mathbf{x}_2, \mathbf{R}_1 \mathbf{R}_2). \quad (4)$$

These roto-translations act transitively over the space $\mathbb{R}^d \times S^{d-1}$ by

$$(\mathbf{x}, \mathbf{R}) \odot (\mathbf{y}, \mathbf{n}) := (\mathbf{x} + \mathbf{R}\mathbf{y}, \mathbf{R}\mathbf{n}), \quad (5)$$

for all $(\mathbf{y}, \mathbf{n}) \in \mathbb{R}^d \times S^{d-1}$ and all roto-translations $(\mathbf{x}, \mathbf{R}) \in SE(d)$.

We choose an *a priori reference vector* $\mathbf{a} \in S^{d-1}$, say $\mathbf{a} = (1, 0)^T$ if $d = 2$ or $\mathbf{a} = (0, 0, 1)^T$ if $d = 3$. Then the stabilizer of the element $(0, \mathbf{a})$ is given by

$$H_d = \{g \in SE(d) \mid g \odot (\mathbf{0}, \mathbf{a}) = (\mathbf{0}, \mathbf{a})\}. \quad (6)$$

which is isomorphic to $SO(d-1)$.

The homogeneous space of positions and orientations is, as a set, just the set of left-cosets

$$\mathbb{M}_d := \mathbb{R}^d \rtimes S^{d-1} := SE(d)/H_d,$$

i.e. they are the equivalence classes in $SE(d)$ with respect to the equivalence relation

$$g_1 \sim g_2 \iff g_1^{-1}g_2 \in H_d.$$

For $d = 2$, the manifold \mathbb{M}_d is diffeomorphic to $SE(d)$, but for $d > 2$ the manifolds are not diffeomorphic.

For $d = 3$, the stabilizer can be described by

$$H_3 = \left\{ h_\alpha := (\mathbf{0}, \mathbf{R}_{\mathbf{a}, \alpha}) \mid \alpha \in [0, 2\pi) \right\},$$

where $\mathbf{R}_{\mathbf{a}, \alpha}$ denotes a (counter-clockwise) rotation over angle α around the reference axis \mathbf{a} . This means that two roto-translations $g_1 = (\mathbf{x}_1, \mathbf{R}_1)$ and $g_2 = (\mathbf{x}_2, \mathbf{R}_2)$ are equivalent if and only if

$$g_1 \sim g_2 \iff \mathbf{x}_1 = \mathbf{x}_2 \text{ and } \exists \alpha \in [0, 2\pi) : \mathbf{R}_1 = \mathbf{R}_2 \mathbf{R}_{\mathbf{a}, \alpha}.$$

The equivalence classes $[g] = \{g' \in SE(3) \mid g' \sim g\}$ are usually just denoted by $p = (\mathbf{x}, \mathbf{n})$ as they consist of all rigid body motions $g = (\mathbf{x}, \mathbf{R}_n)$ that map reference point $(\mathbf{0}, \mathbf{a})$ onto $(\mathbf{x}, \mathbf{n}) \in \mathbb{R}^3 \rtimes S^2$:

$$g \odot (\mathbf{0}, \mathbf{a}) = (\mathbf{x}, \mathbf{n}).$$

Remark 3 (Distinguishing $SE(d)$ from \mathbb{M}_d)

As the distinction between the group $SE(d)$ and the homogeneous space \mathbb{M}_d (which is not a group for $d > 2$) is important, we will use g, h for elements of $SE(d)$, and p, q for points in \mathbb{M}_d .

Remark 4 (Domain of an orientation score)

Due to the axial symmetry assumption on the wavelets, see[27] the orientation score is well-defined on the domain \mathbb{M}_d .

2.3 Differential Structure on $SE(d)$, \mathbb{M}_d

As a manifold, we view the group $SE(d)$ in a standard way as a submanifold of $\mathbb{R}^d \times \mathbb{R}^{d \times d}$. The Lie algebra is, as a vector space, the tangent space at the identity. We view elements of tangent spaces (i.e. tangent vectors) as derivations acting on functions: if v is an ordinary vector in $\mathbb{R}^d \times \mathbb{R}^{d \times d}$ tangent to $SE(d)$, the corresponding derivation acting on a function f is just the derivative of f in the direction of v .

The Lie algebra has dimension $D = \frac{1}{2}d(d+1)$. We choose a basis $(A_i)_{i=1}^D$ for the Lie algebra of $SE(d)$ with the following properties. The basis is orthonormal with respect to the inner product induced by the standard Euclidean metric on $\mathbb{R}^d \times \mathbb{R}^{d \times d}$, the vectors A_1, \dots, A_d form a basis of \mathbb{R}^d , the vector A_d corresponds to the derivative in the direction of \mathbf{a} , the vectors A_{2d}, \dots, A_D are a basis of the stabilizer H_d , and the vector A_i commutes with A_{i+d} for $i = 1, \dots, d$. Thereby the Lie algebra vector A_{i+d} generates the in-plane rotation in the plane spanned by A_i and \mathbf{a} for $i = 1, \dots, d-1$.

Summarized we have the following basis for the Lie algebra:

$$\underbrace{A_1, \dots, A_d}_{\text{spatial generators}}, \underbrace{A_{d+1}, \dots, A_{2d-1}}_{\text{relevant rotation generators}}, \underbrace{A_{2d}, \dots, A_D}_{\text{rotation generators of } H_d}.$$

We extend the vectors A_i to left-invariant vector fields \mathcal{A}_i as follows. The group acts on itself by left multiplication,

$$L_g h := gh, \quad \forall g, h \in SE(d), \quad (7)$$

and the derivation $(\mathcal{A}_i)_g$, evaluated in a point g , is given by the pushforward

$$\mathcal{A}_i|_g f := ((L_g)_* \mathcal{A}_i) f = \mathcal{A}_i(f \circ L_g), \quad (8)$$

for all $f \in C^\infty(SE(d), \mathbb{R})$. We denote the corresponding covector fields by $\omega^i : g \mapsto \omega^i|_g$. For each $g \in SE(d)$, the covector $\omega^i|_g$ is an element of the dual to the tangent space of $SE(d)$ at g . The covector fields are characterized by

$$\langle \omega^i, \mathcal{A}_j \rangle = \delta_j^i, \quad (9)$$

where δ_j^i denotes the Kronecker delta.

Note that

$$A_d = \mathbf{a} \cdot \nabla_{\mathbb{R}^d} \Big|_e = \sum_{i=1}^d a^i \frac{\partial}{\partial x^i} \Big|_e, \quad (10)$$

and so for all $g = (\mathbf{x}, \mathbf{R}_n) \in SE(d)$:

$$\begin{aligned} \mathcal{A}_d \Big|_g &= (L_g)_* A_d = \sum_{i=1}^d (\mathbf{R}_n \mathbf{a})^i \frac{\partial}{\partial x^i} \Big|_g \\ &= \sum_{i=1}^d n^i \frac{\partial}{\partial x^i} \Big|_g = \mathbf{n} \cdot \nabla_{\mathbb{R}^d} \Big|_g. \end{aligned} \quad (11)$$

Meaning that the left invariant frame is aligned with the direction $\mathbf{n} \in S^{d-1}$.

Remark 5 (Left Invariant Basis in 2D)

We can represent an element of $SE(2)$ by its position and angle as $(\mathbf{x}, \theta) \in \mathbb{R}^d \times [0, 2\pi)$ which allows us to write the left-invariant vector fields \mathcal{A}_i as:

$$\begin{aligned}\mathcal{A}_1|_{(\mathbf{x}, \theta)} &= -\sin \theta \partial_x|_{(\mathbf{x}, \theta)} + \cos \theta \partial_y|_{(\mathbf{x}, \theta)}, \\ \mathcal{A}_2|_{(\mathbf{x}, \theta)} &= \cos \theta \partial_x|_{(\mathbf{x}, \theta)} + \sin \theta \partial_y|_{(\mathbf{x}, \theta)} = \mathbf{n} \cdot \nabla_{\mathbb{R}^2}|_g, \\ \mathcal{A}_3|_{(\mathbf{x}, \theta)} &= \partial_\theta.\end{aligned}$$

For an explicit form of the left-invariant vector fields \mathcal{A}_i in case $d = 3$, see Appendix A.

We introduce the following metric tensor field in terms of the left invariant co-vector fields $(\omega^i)_{i=1}^{2d-1}$.

Definition 1 (Left-invariant metric tensor field) Given positive constants $D_S > 0$ and $D_A > 0$, and a nonnegative real number $\epsilon \geq 0$, we define the left-invariant metric tensor field \mathcal{G} by

$$\mathcal{G} = \begin{cases} \frac{\omega^d \otimes \omega^d}{D_S} + \frac{\sum_{i=1}^{d-1} \omega^i \otimes \omega^i}{\epsilon^2 D_S} + \frac{\sum_{i=d+1}^{2d-1} \omega^i \otimes \omega^i}{D_A} & \text{if } \epsilon > 0, \\ \frac{\sum_{i=1}^{d-1} \omega^i \otimes \omega^i}{D_S} & \text{if } \epsilon = 0. \end{cases} \quad (12)$$

Henceforth we refer to ϵ as the sub-Riemannian case where tangent vectors are constrained to the span of $\mathcal{A}_d, \dots, \mathcal{A}_{2d-1}$. Intuitively when $\epsilon \downarrow 0$ the other tangent directions get infinite cost and become prohibited.

Remark 6 (Metric is defined on a sub-bundle)

Observe that this metric tensor is defined (and invertible) on a sub-bundle of the tangent bundle on the group as it does not contain any of the covectors dual to the sub-bundle induced by subgroup H_d . Furthermore it is spatially isotropic orthogonal to the primary spatial direction. Also spherically we impose isotropy in the metric as can be seen from the last term in the above definition.

This metric induces an associated norm: if $\dot{g} \in T_g(SE(d))$, then

$$\|\dot{g}\|_{\mathcal{G}} := \sqrt{\mathcal{G}|_g(\dot{g}, \dot{g})}. \quad (13)$$

Now that we have $SE(d)$ equipped with a (sub -) Riemannian metric tensor we can derive the basic tools we need to formulate geometric PDEs: the gradient, its norm and the divergence of a vector field. If we relabel our parameters as

$$D_i = \begin{cases} D_S & \text{if } i = d, \\ \epsilon^2 D_S & \text{if } 1 \leq i \leq d-1, \\ D_A & \text{if } d+1 \leq i \leq 2d-1, \end{cases} \quad (14)$$

the gradient of a differentiable function $\tilde{U} : SE(d) \rightarrow \mathbb{R}$ on the group induced by this metric tensor becomes

$$\nabla_{\mathcal{G}} \tilde{U} = \sum_{i=1}^{2d-1} D_i (\mathcal{A}_i \tilde{U}) \mathcal{A}_i, \quad (15)$$

which has as norm

$$\|\nabla_{\mathcal{G}} \tilde{U}\|_{\mathcal{G}}^2 = \sum_{i=1}^{2d-1} D_i (\mathcal{A}_i \tilde{U})^2. \quad (16)$$

The divergence of a vector field is simply given by

$$\operatorname{div}_{\mathcal{G}} = \sum_{i=1}^{2d-1} \mathcal{A}_i \circ \left(g \mapsto \omega^i|_g \right), \quad (17)$$

this means that if we apply it to a vector field expressed in left invariant frame as $\mathbf{v} = \sum_{i=1}^{2d-1} v^i \mathcal{A}_i$ we have:

$$\operatorname{div}_{\mathcal{G}} \mathbf{v} = \sum_{i=1}^{2d-1} \mathcal{A}_i v^i.$$

2.4 Locally Adaptive Frames on $SE(d)$

As an alternative to the left-invariant frame we can choose a frame (and subsequently metric tensor field) that is adapted to the data (which we also refer to as *gauge frames* in analogy with [20]). Specifically, instead of having the vector field $\mathcal{A}_d = \mathbf{n} \cdot \nabla$ as a static forward direction we want to choose a \mathcal{B}_d vector field that locally aligns with the data [20], in particular \mathcal{B}_d can take on an angular component meaning the local ‘straight forward’ will follow the curve of the data meaning flows can better follow curved structures, see Fig. 3.

Remark 7 (Fitting a frame)

An exponential curve fit induces an entire frame in $SE(d)$, see [20, Appendix A] for details. For an intuitive illustration see Fig. 3. In this article we will focus on the method by which the main gauge vector is obtained.

Next we will explain a singular value decomposition of the Hessian, we will choose the eigenvector associated with the smallest eigenvalue as \mathcal{B}_d . Geometrically this can be seen as the direction in which the gradient changes the least. Before we can formulate this procedure we explain the concept of exponential curves (see Fig. 4).

Definition 2 (Exponential curve) Let $\dot{g} \in T_g(SE(d))$ then the exponential curve parameterized by t through g with tangent vector \dot{g} is written as $e_g^{\dot{g}t}$ and is the curve for which $e_g^{\dot{g}0} = g$ and which has the property that for all $t \in \mathbb{R}$:

$$\left(\frac{d}{dt} e_g^{\dot{g}t} \right) (t) = \sum_{i=1}^{2d-1} \omega^i|_g(\dot{g}) \mathcal{A}_i|_{e_g^{\dot{g}t}}.$$

Or more explicitly in coordinates, if $\dot{g} = \sum_{i=1}^{2d-1} \dot{g}^i \mathcal{A}_i|_g$ we have that:

$$\left(\frac{d}{dt} e_g^{\dot{g}t} \right) (t) = \sum_{i=1}^{2d-1} \dot{g}^i \mathcal{A}_i|_{e_g^{\dot{g}t}}.$$

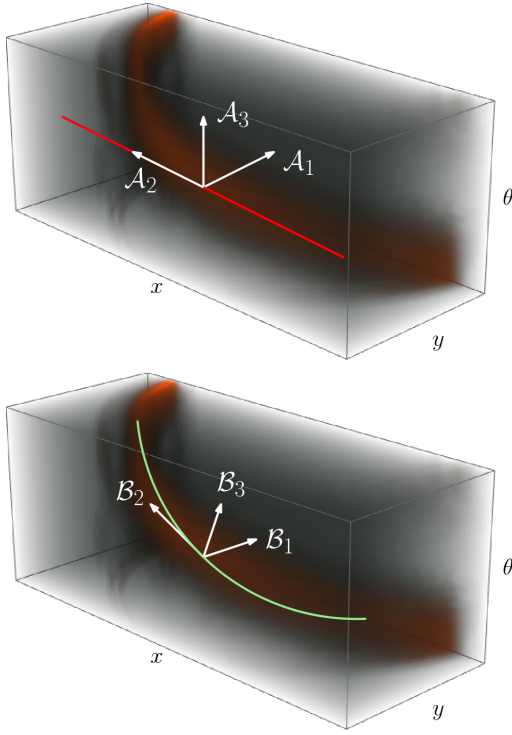


Fig. 3: Illustrating gauge frame fitting. Top: left invariant frame where $\mathcal{A}_d = \mathbf{n} \cdot \nabla_{\mathbb{R}^2}$, recall (11), as indicated by the red line. Bottom: we choose a frame that takes into account the local curvature.

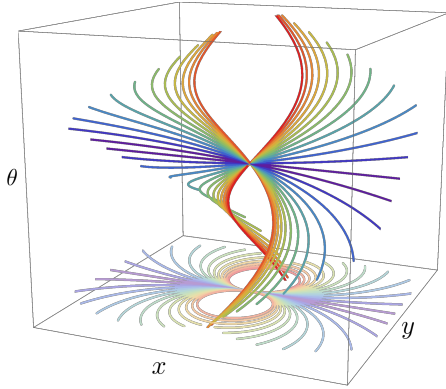


Fig. 4: A set of exponential curves through a common point for $d = 2$. Exponential curves are those curves whose tangent vectors are part of a left invariant vector field. Taken with permission from [7].

Hence the exponential curves are those curves whose tangent vector components with respect to the left invariant frame do not change. For an illustration of such curves for the case $d = 2$ see Fig. 4.

Now we want to select $\mathcal{B}_d|_g$ (normalized with respect to the existing metric tensor $\mathcal{G}|_g$) so that the gradient of the data $\tilde{U} \in C^1(SE(d), \mathbb{R})$ changes as little as possible (recall Fig. 3) in the following manner.

Definition 3 (Main gauge vector) We define the main gauge vector as

$$\begin{aligned} \mathcal{B}_d|_g &:= \operatorname{argmin}_{\substack{\dot{g} \in T_g(SE(d)) \\ \|\dot{g}\|_{\mathcal{G}}=1}} \left\| \frac{d}{dt} \left[\left(L_{g(e_g^{\dot{g}})}^{-1} \right)_* \nabla_{\mathcal{G}} \tilde{U} (e_g^{\dot{g}}) \right] \Big|_{t=0} \right\|_{\mathcal{G}}^2 \\ &= \operatorname{argmin}_{\substack{\dot{g} \in T_g(SE(d)) \\ \|\dot{g}\|_{\mathcal{G}}=1}} \left\| \lim_{t \rightarrow 0} \frac{\left(L_{g(e_g^{\dot{g}})}^{-1} \right)_* \nabla_{\mathcal{G}} \tilde{U} (e_g^{\dot{g}}) - \nabla_{\mathcal{G}} \tilde{U} (g)}{t} \right\|_{\mathcal{G}}^2. \end{aligned}$$

Writing the tangent vector in terms of the local left invariant frame as $\dot{g} = \sum_{i=1}^{2d-1} \dot{g}^i \mathcal{A}_i|_g$ gives

$$\begin{aligned} \mathcal{B}_d|_g &= \operatorname{argmin}_{\substack{\dot{g} \in T_g(SE(d)) \\ \|\dot{g}\|_{\mathcal{G}}=1}} \sum_{i=1}^{2d-1} D_i (\dot{g}^i \mathcal{A}_i \tilde{U})^2 \\ &= \operatorname{argmin}_{\substack{\dot{g} \in T_g(SE(d)) \\ \|\dot{g}\|_{\mathcal{G}}=1}} \sum_{i=1}^{2d-1} D_i \left(\sum_{j=1}^{2d-1} \dot{g}^j \mathcal{A}_j (\mathcal{A}_i \tilde{U}) \right)^2. \end{aligned} \quad (18)$$

We can write this problem in terms of matrices by defining the following:

$$\begin{aligned} \dot{\mathbf{g}} &= (\dot{g}^1, \dot{g}^2, \dots, \dot{g}^{2d-1})^T, \\ M &= \operatorname{diag}(\sqrt{D_1}, \sqrt{D_2}, \dots, \sqrt{D_{2d-1}}), \\ K &= K(\tilde{U})|_g := (\mathcal{A}_j|_g (\mathcal{A}_i|_g \tilde{U}))_{i,j}. \end{aligned}$$

with i as row index and j as column index.

Using these the objective function in (18) becomes

$$(MK\dot{\mathbf{g}})^T (MK\dot{\mathbf{g}}) = \dot{\mathbf{g}}^T K^T M^2 K \dot{\mathbf{g}}, \quad (19)$$

which we want to minimize under the constraint

$$\sum_{i=1}^{2d-1} \frac{(\dot{g}^i)^2}{D_i} = \|M^{-2}\dot{\mathbf{g}}\|^2 = 1. \quad (20)$$

Taking the derivative of the Lagrangian of this convex optimization problem gives us optimality under the following condition ($\lambda \in \mathbb{R}$):

$$K^T M^2 K \dot{\mathbf{g}} = \lambda M^{-2} \dot{\mathbf{g}} \iff M^2 K^T M^2 K \dot{\mathbf{g}} = \lambda \dot{\mathbf{g}}, \quad (21)$$

i.e. $\dot{\mathbf{g}}$ needs to be an eigenvector of the matrix $M^2 K^T M^2 K$ with eigenvalue λ (serving as the Lagrangian multiplier). If for a moment we rewrite (21) as

$$(MKM)^T (MKM) (M^{-1}\dot{\mathbf{g}}) = \lambda (M^{-1}\dot{\mathbf{g}}), \quad (22)$$

we see that λ is indeed real since $(MKM)^T(MKM)$ is symmetric. With this eigenvalue and vector the objective function (19) evaluates to

$$\begin{aligned}\dot{\mathbf{g}}^T K^T M^2 K \dot{\mathbf{g}} &= \dot{\mathbf{g}}^T M^{-2} M^2 K^T M^2 K \dot{\mathbf{g}} \\ &= \dot{\mathbf{g}}^T M^{-2} \lambda \dot{\mathbf{g}} \\ &= \lambda \dot{\mathbf{g}}^T M^{-2} \dot{\mathbf{g}} \\ &= \lambda \|\dot{\mathbf{g}}\|_{\mathcal{G}}^2 = \lambda.\end{aligned}$$

Which incidentally proves that $M^2 K^T M^2 K$ is positive semi-definite and, more importantly, that to minimize the change in gradient we need to look at the eigenvector belonging to the smallest eigenvalue.

In practice, we do not immediately calculate the eigenvectors and eigenvalues from the scheme we have just proposed, but for the purpose of stability we first apply a component-wise Gaussian smoothing on the matrix K as follows:

$$\begin{aligned}\tilde{K}|_g &:= (G * K)(\mathbf{x}, \mathbf{R}_n) \\ &= \int_{\mathbb{R}^d} \int_{S^{d-1}} G(\mathbf{x} - \mathbf{y}, R_{\mathbf{m}}^T \mathbf{n}) K|_{(\mathbf{y}, \mathbf{R}_m)} d\sigma(\mathbf{m}) dy,\end{aligned}\quad (23)$$

with the usual surface measure σ on S^{d-1} and with the smoothing function

$$G(\mathbf{y}, \mathbf{m}) := G_{\rho_s}^{\mathbb{R}^d}(\mathbf{y}) \cdot G_{\rho_a}^{S^{d-1}}(\mathbf{m}), \quad (24)$$

where G_{ρ}^M is the isotropic heat kernel on manifold M with scale $\rho > 0$. Isotropic diffusion is important since it is the only diffusion that commutes with the left invariant vector fields. Note that $G_{\mathbb{R}^d}(\mathbf{y})$ depends only on $\|\mathbf{y}\|$ and $G^{S^{d-1}}(\mathbf{m})$ depends only on $\arccos(\mathbf{a} \cdot \mathbf{m})$. This smoothing method is a variant on the one used in [20].

The remaining basis vectors are determined by looking at a rotation that maps $\mathcal{A}_d|_g$ to $\mathcal{B}_d|_g$ and then applying a specific rotation to the remaining $\mathcal{A}_i|_g$ that keeps the remaining spatial generators spatial. For an illustration see Fig. 3. How this rotation is chosen and applied is detailed in [20, App.B].

Having determined a data adaptive frame $(\mathcal{B}_i)_{i=1}^{2d-1}$ (induced by \mathcal{B}_d , recall Fig. 3) we equip it with the following straightforward metric, where again we rely on the corresponding dual frame $(\beta^i)_{i=1}^{2d-1}$ given by

$$\langle \beta^i, \mathcal{B}_j \rangle = \delta_j^i. \quad (25)$$

Definition 4 (Gauge Metric Tensor Field)

We define the gauge metric tensor field $g \mapsto \mathcal{J}|_g(\cdot, \cdot)$ as

$$\mathcal{J} := \sum_{i=1}^{2d-1} \beta^i \otimes \beta^i. \quad (26)$$

Which induces a norm on $\dot{g} \in T_g(SE(d))$:

$$\|\dot{g}\|_{\mathcal{J}} := \sqrt{\mathcal{J}|_g(\dot{g}, \dot{g})}, \quad (27)$$

a gradient on $\tilde{U} \in C^1(SE(d))$:

$$\nabla_{\mathcal{J}} \tilde{U} := \sum_{i=1}^{2d-1} (\mathcal{B}_i \tilde{U}) \mathcal{B}_i, \quad (28)$$

with norm

$$\|\nabla_{\mathcal{J}} \tilde{U}\|_{\mathcal{J}}^2 = \sum_{i=1}^{2d-1} (\mathcal{B}_i \tilde{U})^2, \quad (29)$$

and finally gives the divergence of a vector field as:

$$\operatorname{div}_{\mathcal{J}} = \sum_{i=1}^{2d-1} \mathcal{B}_i \circ (g \mapsto \beta^i|_g), \quad (30)$$

which means that if we apply it to a vector field expressed in the gauge frame as $\mathbf{u} = \sum_{i=1}^{2d-1} u^i \mathcal{B}_i$ we have:

$$\operatorname{div}_{\mathcal{J}} \mathbf{u} = \sum_{i=1}^{2d-1} \mathcal{B}_i u^i.$$

2.5 Coherence Enhancement Operator

Coherence enhancing diffusion is a well-known technique for image enhancement [39], it is intended for line amplification rather than strictly denoising. Crossing preserving versions on \mathbb{M}_d have been developed [20] and evaluated for denoising. Here crossing lines are well-enhanced but plateaus and boundaries of line structures are damaged. Therefore we propose to include the coherence enhancement technique into TV and MC flows.

Next we explain how this coherence enhancement operator is constructed from an orientation confidence.

In \mathbb{R}^3 orientation confidence is calculated by the Laplacian in the subspace orthogonal to the line structure, we can take a similar approach in \mathbb{M}_d by taking the Laplacian in the space spanned by $(\mathcal{A}_i)_{i=1, i \neq d}^{2d-1}$. Recall that \mathcal{A}_d is implicitly aligned with the local line structure along \mathbf{n} . In the gauge frame setting \mathcal{B}_d is explicitly aligned with the line structure (see Fig. 3) and therefore we take the Laplacian in the span of $(\mathcal{B}_i)_{i=1, i \neq d}^{2d-1}$.

In the sub-Riemannian case (i.e. $D_1 = \dots = D_{d-1} = 0$) this just reduces to the second derivatives in the $d-1$ -dimensional spaces spanned by $(\mathcal{A}_i)_{i=d+1}^{2d-1}$ and $(\mathcal{B}_i)_{i=d+1}^{2d-1}$ respectively. With that in mind we define orientation confidence in $SE(d)$ as follows.

Let $\tilde{U} : SE(d) \rightarrow \mathbb{R}$, then in the left invariant case we define

$$C_{\tilde{U}}(g) := \left| \sum_{i=1, i \neq d}^{2d-1} D_i \mathcal{A}_i \Big|_g (\mathcal{A}_i \tilde{U}) \right|, \quad (31)$$

or

$$:= \left| \sum_{i=1, i \neq d}^{2d-1} \mathcal{B}_i \Big|_g (\mathcal{B}_i \tilde{U}) \right|. \quad (32)$$

in the gauge frame case.

Note that the \mathcal{B}_i 's are normalized with respect to the old metric (12) and as such the parameters D_i are still included in (32). In the case that $\mathcal{B}_d \simeq \mathcal{A}_d$ we have $\mathcal{B}_i = \sqrt{D_i} \mathcal{A}_i$ and (31) & (32) coincide.

Definition 5 (Isotropy factor) Let $c > 0$ be a chosen scaling constant, then the isotropy factor is defined as:

$$\alpha_{\tilde{U}}(g) := e^{-\frac{C_{\tilde{U}}(g)}{c}},$$

with $C_{\tilde{U}}$ defined by (31) respectively (32).

What is convenient about this quantity is that it gives a number in the range $(0, 1]$ with a number close to zero indicating a high degree of anisotropy and a 1 indicating perfect isotropy, this is the quantity that we can use to steer flow.

The choice of c controls how steep the decline of the isotropy factor is, its appropriate value depends on the application and on exactly how the data is represented numerically (normalized to $[0, 1]$ in our case) and is best determined heuristically or by histogram. For our experiments we have used $c = 0.2$.

Using this scalar function $\alpha_{\tilde{U}}$ over the group $SE(d)$ we can locally modify vectors based on how certain we are the data is locally aligned. We refer to this modification of vector fields as *coherence enhancement* (as in coherence enhancing diffusion [24]). Tangent vectors (such as the gradient as we will see) are modified as follows, let \mathbf{v} be a vector field on $SE(d)$ then the coherence enhanced vector field is given as (for the left invariant geometry):

$$E_{\mathcal{G}}(\mathbf{v}) := \langle \boldsymbol{\omega}^d, \mathbf{v} \rangle \mathcal{A}_d + \alpha_{\tilde{U}} \sum_{\substack{i=1 \\ i \neq d}}^{2d-1} \langle \boldsymbol{\omega}^d, \mathbf{v} \rangle \mathcal{A}_i, \quad (33)$$

and for the gauge geometry:

$$E_{\mathcal{J}}(\mathbf{v}) := \langle \boldsymbol{\beta}^d, \mathbf{v} \rangle \mathcal{B}_d + \alpha_{\tilde{U}} \sum_{\substack{i=1 \\ i \neq d}}^{2d-1} \langle \boldsymbol{\beta}^d, \mathbf{v} \rangle \mathcal{B}_i. \quad (34)$$

Intuitively these linear operators $E_{\mathcal{G}}, E_{\mathcal{J}} : T(G) \rightarrow T(G)$ keep the magnitude of the vector in the main direction and weaken it orthogonal to the main direction if we are certain the data is locally aligned to the main direction.

2.6 Descending to the Homogeneous Space

So far we have developed two distinct geometries on the group $SE(d)$ that are summarized in Table 1. We can bring these geometries down to the homogeneous space \mathbb{M}_d by considering the natural extension of functions and vector fields on \mathbb{M}_d to $SE(d)$. Consider a function U on \mathbb{M}_d then the function \tilde{U} given by

$$\tilde{U}(g) = \tilde{U}(\mathbf{x}, \mathbf{R}) := U(\mathbf{x}, \mathbf{R}\mathbf{a}) \quad (35)$$

for all $g = (\mathbf{x}, \mathbf{R}) \in SE(d)$, is its natural extension to $SE(d)$. Similarly a tangent vector field (recall that we understand these as differential operators acting on scalar functions) \mathbf{v} on \mathbb{M}_d can be extended as follows:

$$(\tilde{\mathbf{v}}\tilde{U})(g) = (\tilde{\mathbf{v}}\tilde{U})(\mathbf{x}, \mathbf{R}) := (\mathbf{v}U)(\mathbf{x}, \mathbf{R}\mathbf{a}), \quad (36)$$

under the additional constraint that $\tilde{\mathbf{v}}$ vanishes in the direction induced by the subgroup H_d (i.e. for all $i \geq 2d$ we have $\langle \boldsymbol{\omega}^i, \tilde{\mathbf{v}} \rangle = 0$) this extension is unique.

Having extended functions and vector fields upward to the group we can apply the tools from Table 1 to them and subsequently project the results back to the homogeneous space by the mapping $(\mathbf{x}, \mathbf{R}) \mapsto (\mathbf{x}, \mathbf{R}\mathbf{a})$. This mapping is not injective. Nevertheless thanks to the metrics (12)(26) being isotropic laterally and spherically and the way we extend functions to the group by (35)(36) all the tools we list in Table 2 are well-defined on \mathbb{M}_d .

Choice of geometry	Left invariant	Gauge
Frame	$\mathcal{A}_1, \mathcal{A}_2, \dots, \mathcal{A}_{2d-1}$	$\mathcal{B}_1, \mathcal{B}_2, \dots, \mathcal{B}_{2d-1}$
Co-frame	$\boldsymbol{\omega}^1, \boldsymbol{\omega}^2, \dots, \boldsymbol{\omega}^{2d-1}$	$\boldsymbol{\beta}^1, \boldsymbol{\beta}^2, \dots, \boldsymbol{\beta}^{2d-1}$
Metric tensor	\mathcal{G}	\mathcal{J}
Gradient ∇	$\nabla_{\mathcal{G}}$	$\nabla_{\mathcal{J}}$
Divergence div	$\sum_{i=1}^{2d-1} \mathcal{A}_i \circ \boldsymbol{\omega}^i$	$\sum_{i=1}^{2d-1} \mathcal{B}_i \circ \boldsymbol{\beta}^i$
Norm $\ \cdot\ $	$\ \cdot\ _{\mathcal{G}}$	$\ \cdot\ _{\mathcal{J}}$
Volume form $d\bar{\mu}$	$\frac{\boldsymbol{\omega}^1 \wedge \boldsymbol{\omega}^2 \wedge \dots \wedge \boldsymbol{\omega}^{2d-1}}{\sqrt{D_S} \sqrt{\epsilon D_S D_A}^{d-1}}$	$\boldsymbol{\beta}^1 \wedge \boldsymbol{\beta}^2 \wedge \dots \wedge \boldsymbol{\beta}^{2d-1}$

Table 1: We formulate our PDEs independent of our choice of frame and metric and then apply it to both the left invariant and gauge geometries.

Remark 8 (Choice of \mathbf{R}_n)

While the choice of mapping $\mathbf{n} \mapsto \mathbf{R}_n$ does not matter for the final result, a choice does have to be made for an implementation when $d \geq 3$. The most straightforward manner is selecting that \mathbf{R}_n which is an in-plane rotation, meaning the plane of rotation is spanned by \mathbf{a} and \mathbf{n} . In the two cases where this is not possible (i.e. $\mathbf{n} = \pm \mathbf{a}$) we pick $\mathbf{R}_a = \mathbf{0}$ and $\mathbf{R}_{-\mathbf{a}} = \mathbf{R}_{\mathbf{e}_y, \pi}$, where $\mathbf{R}_{\mathbf{e}_y, \pi}$ denotes the rotation around the axis \mathbf{e}_y by an angle π . Concretely the in-plane rotation in

\mathbb{M}_d tools	Left invariant	Gauge
$\nabla U(\mathbf{x}, \mathbf{n}) =$	$(\nabla_{\mathcal{G}} \tilde{U})(\mathbf{x}, \mathbf{R}_n)$	$(\nabla_{\mathcal{J}} \tilde{U})(\mathbf{x}, \mathbf{R}_n)$
$(\mathbf{v}, \mathbf{w})_{\mathbb{M}_d} \Big _{(\mathbf{x}, \mathbf{n})} =$	$\mathcal{G} \Big _{(\mathbf{x}, \mathbf{R}_n)}(\tilde{\mathbf{v}}, \tilde{\mathbf{w}})$	$\mathcal{J} \Big _{(\mathbf{x}, \mathbf{R}_n)}(\tilde{\mathbf{v}}, \tilde{\mathbf{w}})$
$\ \mathbf{v}\ _{\mathbb{M}_d} =$	$\ \tilde{\mathbf{v}}\ _{\mathcal{G}}$	$\ \tilde{\mathbf{v}}\ _{\mathcal{J}}$
$(\operatorname{div} \mathbf{v})(\mathbf{x}, \mathbf{n}) =$	$(\operatorname{div}_{\mathcal{G}} \tilde{\mathbf{v}})(\mathbf{x}, \mathbf{R}_n)$	$(\operatorname{div}_{\mathcal{J}} \tilde{\mathbf{v}})(\mathbf{x}, \mathbf{R}_n)$
$d\mu(\mathbf{x}, \mathbf{n}) =$	$d\tilde{\mu}_{\mathcal{G}}(\mathbf{x}, \mathbf{R}_n)$	$d\tilde{\mu}_{\mathcal{J}}(\mathbf{x}, \mathbf{R}_n)$
$(E\mathbf{v})(\mathbf{x}, \mathbf{n})$	$(E_{\mathcal{G}} \tilde{\mathbf{v}})(\mathbf{x}, \mathbf{R}_n)$	$(E_{\mathcal{J}} \tilde{\mathbf{v}})(\mathbf{x}, \mathbf{R}_n)$

Table 2: The two geometries we developed on $SE(d)$ can be naturally applied to the homogeneous space \mathbb{M}_d using the natural extension of scalar functions (35) and vector fields (36). These objects are well defined despite the non-injective mapping used since the choice of particular $\mathbf{R}_n \in SE(d)$ that maps \mathbf{a} to \mathbf{n} does not affect any of them.

3D are given in terms of the ZYZ-Euler angles α, β, γ by requiring that $\alpha = -\gamma$, which gives the mapping

$$\mathbf{n} \mapsto \mathbf{R}_{\mathbf{e}_z, -\alpha} \mathbf{R}_{\mathbf{e}_y, \beta} \mathbf{R}_{\mathbf{e}_z, \alpha}, \quad (37)$$

for the unique $\alpha \in [0, 2\pi)$ and $\beta \in (0, \pi)$ so that the resulting rotation maps \mathbf{a} to \mathbf{n} .

3 Total Variation, Mean Curvature PDE Flows on \mathbb{M}_d

3.1 PDE System

On \mathbb{R}^n the formulation of total variation is built on the identity $\operatorname{div}(f\mathbf{v}) = f \operatorname{div}(\mathbf{v}) + \nabla f \cdot \mathbf{v}$. Similarly on \mathbb{M}_d we have:

$$\begin{aligned} \operatorname{div}(U\mathbf{v}) &= U \operatorname{div}(\mathbf{v}) + dU(\mathbf{v}) \\ &= U \operatorname{div}(\mathbf{v}) + (\nabla U, \mathbf{v})_{\mathbb{M}_d}. \end{aligned} \quad (38)$$

From which we deduce the following integration by parts formula:

$$\int_{\Omega} U(p) \operatorname{div} \mathbf{v}(p) d\mu(p) = \int_{\Omega} (\nabla U(p), \mathbf{v}(p))_{\mathbb{M}_d} d\mu(p), \quad (39)$$

for all $U \in C^1(\Omega)$ and all smooth vector fields \mathbf{v} vanishing at the boundary $\partial\Omega$. This formula allows us to build a weak formulation of TVF on \mathbb{M}_d .

Definition 6 (weak formulation of TVF on \mathbb{M}_d)

Let $U \in BV(\Omega)$ be a function of bounded variation. Let $\chi_0(\Omega)$ denote the vector space of smooth vector fields that vanish at the boundary $\partial\Omega$. Then we define

$$TV_{\varepsilon}(U) := \sup_{\substack{\psi \in C_c^{\infty}(\Omega) \\ \mathbf{v} \in \chi_0(\Omega) \\ \|\mathbf{v}(p)\|_{\varepsilon}^2 + |\psi(p)|^2 \leq 1}} \int_{\Omega} \begin{pmatrix} \varepsilon \\ U(p) \end{pmatrix} \cdot \begin{pmatrix} \psi(p) \\ \operatorname{div} \mathbf{v}(p) \end{pmatrix} d\mu(p) \quad (40)$$

For all $U \in BV(\Omega)$ we have

$$TV_0(U) \leq TV_{\varepsilon}(U) \leq TV_0(U) + \varepsilon |\Omega|.$$

Lemma 1 Let $\varepsilon \geq 0$. For $U \in C^1(\Omega, \mathbb{R})$ we have

$$TV_{\varepsilon}(U) = \int_{\Omega} \sqrt{\|\nabla U(p)\|_{\mathbb{M}_d}^2 + \varepsilon^2} d\mu(p). \quad (41)$$

Furthermore for $U \in C^2(\mathbb{M}_d, \mathbb{R})$ and $\varepsilon, \delta > 0$ we have that

$$\partial TV_{\varepsilon}(U) = \operatorname{div} \circ \left(\frac{\nabla U}{\sqrt{\|\nabla U\|_{\mathbb{M}_d}^2 + \varepsilon^2}} \right). \quad (42)$$

Proof First we substitute (39) into (40), then we apply Gauss theorem and use $U\mathbf{v}|_{\partial\Omega} = 0$. Then we apply Cauchy-Schwarz on $V_p := \mathbb{R} \times T_p\mathbb{M}_d$ for each $p \in \mathbb{M}_d$, with inner product

$$(\varepsilon_1, \mathbf{v}_1) \cdot (\varepsilon_2, \mathbf{v}_2) = \varepsilon_1 \varepsilon_2 + (\mathbf{v}_1, \mathbf{v}_2)_{\mathbb{M}_d},$$

which holds with equality iff the vectors are linearly dependent. Therefore we smoothly approximate

$$\frac{1}{\sqrt{\varepsilon^2 + \|\nabla U\|_{\mathbb{M}_d}^2}}(\varepsilon, \nabla U)$$

by (ψ, \mathbf{v}) to get (41).

For $U \in C^2(\Omega, \mathbb{R})$, $\delta \in C_c^{\infty}(\Omega, \mathbb{R})$ we get

$$\begin{aligned} (\partial TV_{\varepsilon}(U), \delta)_{L_2(\Omega)} &= \lim_{h \downarrow 0} \frac{TV_{\varepsilon}(U + h\delta) - TV_{\varepsilon}(U)}{h} \\ &\stackrel{(39)}{=} \left(\operatorname{div} \circ \left(\frac{\nabla U}{\sqrt{\|\nabla U\|_{\mathbb{M}_d}^2 + \varepsilon^2}} \right), \delta \right)_{L_2(\Omega)}, \end{aligned}$$

and the result follows. \square

For vector fields \mathbf{v} on \mathbb{M}_d define the regularized norm:

$$\|\mathbf{v}\|_{\varepsilon} := \sqrt{\|\mathbf{v}\|_{\mathbb{M}_d}^2 + \varepsilon^2}. \quad (43)$$

This is a common way to regularize denominators and we will use Section 4 to prove that this approach converges for $\varepsilon \rightarrow 0$.

Now we propose the following roto-translation equivariant enhancement PDE on $\Omega \subset \mathbb{M}_d$, recall (1).

Definition 7 (Equivariant Enhancement PDE) Given $U \in BV(\Omega)$ with $\varepsilon > 0$ then we call $W^\varepsilon : \mathbb{M}_d \times \mathbb{R}_{\geq 0} \rightarrow \mathbb{R}$ (being smooth) obeying

$$\begin{cases} \frac{\partial W^\varepsilon}{\partial t}(p, t) = \|\nabla W^\varepsilon\|_\varepsilon^a \operatorname{div} \left(\frac{\nabla W^\varepsilon(\cdot, t)}{\|\nabla W^\varepsilon(\cdot, t)\|_\varepsilon^b} \right)(p) & t \geq 0, \\ \nabla_{\mathbb{R}^2} W^\varepsilon(p, 0) \cdot \mathbf{N}(\mathbf{x}) = 0 & p = (\mathbf{x}, \mathbf{n}) \in \partial\Omega, \\ W^\varepsilon(p, 0) = U(p) & p \in \Omega, \end{cases} \quad (44)$$

the gradient flow started at U with evolution time $t \geq 0$ and parameters $a, b \in \{0, 1\}$. Where we use Neumann boundary conditions with $\mathbf{N}(\mathbf{x})$ as the normal to the spatial boundary at $\mathbf{x} \in \Omega_f$.

The coherence enhancement version of this PDE is given by replacing div by $\operatorname{div} \circ E$ (recall (33) and (34)):

$$\frac{\partial W^\varepsilon}{\partial t}(p, t) = \|\nabla W^\varepsilon\|_\varepsilon^a \operatorname{div} \circ E \left(\frac{\nabla W^\varepsilon(\cdot, t)}{\|\nabla W^\varepsilon(\cdot, t)\|_\varepsilon^b} \right)(p).$$

Remark 9 (Two versions of the PDE)

This PDE system on the quotient \mathbb{M}_d has two versions depending on whether one chooses the left invariant or gauge geometry as outlined in Table 1 and 2.

We then have the following cases:

- For $(a, b) = (1, 1)$ we arrive at Mean Curvature Flow (MCF), studied for $d = 2$ in [12].
- For $(a, b) = (0, 1)$ we arrive at Total Variation Flow, studied for $d = 2$ in [11].
- For $(a, b) = (0, 0)$ we arrive at a linear diffusion for which exact smooth solutions exist for both $d = 2$ and $d = 3$ [31].

Remark 10 (PDE in terms of curvature)

By the product rule (38) the right-hand side of (44) for $\varepsilon \downarrow 0$ becomes

$$\frac{\partial W^0}{\partial t} = \|\nabla W^0\|^{a-b} \Delta W^0 + 2b \bar{\kappa}_T \|\nabla W^0\|^a, \quad (45)$$

with the mean curvature $\bar{\kappa}_T(p, t)$ of level set

$$\{q \in \mathbb{M}_d \mid W^0(q, t) = W^0(p, t)\},$$

akin to [26, ch:3.2], and with (possibly hypo-elliptic) Laplacian $\Delta = \operatorname{div} \circ \nabla$.

Remark 11 (Lack of regularity and weak solutions)

For MCF and TVF smooth solutions to the PDE (44) exist only under special circumstances. This lack of regularity is an advantage in image processing to preserve step-edges

and plateaus in images, yet it forces us to define a concept of weak solutions. Here, we distinguish between MCF and TVF:

For MCF one relies on viscosity solution theory developed by Evans-Spruck [22], see also [25, 35] for the case of MCF with Neumann boundary conditions. In [12, Thm 3.6] existence of C^1 -viscosity solutions is shown for $d = 2$.

For TVF we will rely on gradient flow theory by Brezis-Komura [10, 4].

Convergence of the solutions w.r.t. $\varepsilon \downarrow 0$ is clear from the exact solutions for $(a, b) = (0, 0)$, see [31, ch:2.7], and is also addressed for MCF [12, 6]. For TVF one can rely on [21]. In Section 4 we will therefore only focus on convergence results for $\varepsilon \downarrow 0$.

3.2 Numerics

We implemented the PDE system (44) by Euler forward time discretization, relying on standard B-spline or linear interpolation techniques for derivatives in the underlying tools on \mathbb{M}_d given by table 2. For details see [24, 15]. Also, the explicit upperbounds for stable choices of stepsizes can be derived by the Gershgorin circle theorem [24, 15].

For $d = 2$ the discretization is straightforward [24], for $d = 3$ we discretized per [15] in the software developed by Martin et al. [28], to our PDEs of interest (44) on \mathbb{M}_3 .

The Euler-forward discretizations are not unconditionally stable. For $a = b = 0$, the Gershgorin circle theorem [15, ch.4.2] gives the stability bound

$$\Delta t \leq (\Delta t)_{crit} := \left(\frac{(d-1)D_A + D_S}{2h^2} + \frac{(d-1)D_A}{2h_a^2} \right)^{-1},$$

when using linear interpolation with spatial stepsize h and angular stepsize h_a . In our experiments, for $d = 2$ we set $h = 1$ and for $d = 3$ we took $h_a = \frac{\pi}{25}$ using an almost uniform spherical sampling from a tessellated icosahedron with $N_A = 162$ points. TVF required smaller time steps when ε decreases. Keeping in mind (45) but then applying the product rule (38) to the case $0 < \varepsilon \ll 1$, we concentrate on the first term as it is of order ε^{-1} when the gradient vanishes. Then we find $\Delta t \leq \varepsilon \cdot (\Delta t)_{crit}$ for TVF. For MCF we do not have this limitation.

4 Gradient Flow and Convergence

In this section we provide a gradient flow formulation that we will use to prove the convergence of our regularization scheme for TVF. The reader who is more interested in the experimental results than the technical convergence results can safely choose to skip this section and continue reading Section 5.

4.1 Preliminaries

The total variation flow can be seen as a gradient flow of a lower-semicontinuous, convex functional in a Hilbert space, as we explain next.

If $F : H \rightarrow [0, \infty]$ is a proper (i.e. not everywhere equal to infinity), lower semicontinuous, convex functional on a Hilbert space H (not to be confused with the subgroup H above, as we will not need the subgroup anymore we will stick with convention and use H for the Hilbert space from now on), the subdifferential of F in a point u in the finiteness domain of F is defined as

$$\partial F(u) := \{z \in H \mid (z, v - u) \leq F(v) - F(u) \text{ for all } v \in H\}.$$

The subdifferential is closed and convex, and thereby it has an element of minimal norm, called “the gradient of F in u ” denoted by $\text{grad}F(u)$. Let u_0 be in the closure of the finiteness domain of F . By Brezis-Komura theory, [10], [4, Thm 2.4.15] there is a unique locally absolutely continuous curve $u : [0, \infty) \rightarrow H$ such that

$$-u'(t) = \text{grad}F(u(t)) \text{ for a.e. } t > 0 \text{ and } \lim_{t \downarrow 0} u(t) = u_0.$$

We call $u : [0, \infty) \rightarrow H$ the gradient flow of F starting at u_0 .

Recall the the definition of Ω in (1), then the function $TV_\varepsilon : L^2(\Omega) \rightarrow [0, \infty]$ is lower-semicontinuous and convex for every $\varepsilon \geq 0$. This allows us to generalize solutions to the PDE (44) as follows:

Definition 8 Let $U \in \mathcal{E} := BV(\Omega) \cap \mathbb{L}_2(\Omega)$. We define by $t \mapsto W^\varepsilon(\cdot, t)$ the gradient flow of TV_ε starting at U .

Remark 12 (Smooth solutions)

A smooth solution W^ε to (44) with $(a, b) = (0, 1)$ is a gradient flow.

A functional $\Phi : H \rightarrow (-\infty, \infty]$ is said to be λ -convex for some $\lambda \in \mathbb{R}$ if

$$u \mapsto \Phi(u) - \frac{\lambda}{2} \|u\|^2$$

is convex. In that case, the functional

$$u \mapsto \Phi(u) - \frac{\lambda}{2} \|u - v\|^2$$

is convex as well, for arbitrary $v \in H$, because the latter functional deviates from the first by an affine functional.

We first prove a stability estimate for the minimization of $1/\tau$ -convex functionals.

Lemma 2 Let $\tau > 0$. If a functional $\Phi : H \rightarrow (-\infty, \infty]$ on H is $1/\tau$ -convex, and u^* is its unique minimizer, then for all $u \in H$,

$$\frac{1}{2\tau} \|u - u^*\|^2 \leq \Phi(u) - \Phi(u^*).$$

Proof The functional $\Psi : H \rightarrow (-\infty, \infty]$ given by

$$\Psi(u) := \Phi(u) - \Phi(u^*) - \frac{1}{2\tau} \|u - u^*\|^2$$

is convex. It is sufficient to show that Ψ is nonnegative. If it were not, there would exist a $v \in H$ such that $\Psi(v) < 0$. We will show that then, for t small enough, $\Phi(tv + (1-t)u^*) < \Phi(u^*)$, contradicting that u^* is a minimizer. We first have by definition that, for $t \in (0, 1)$,

$$\begin{aligned} \Phi(tv + (1-t)u^*) - \Phi(u^*) - \frac{t^2}{2\tau} \|v - u^*\|^2 \\ = \Psi(tv + (1-t)u^*). \end{aligned}$$

By the convexity of Ψ ,

$$\begin{aligned} \Psi(tv + (1-t)u^*) &\leq t\Psi(v) + (1-t)\Psi(u^*) \\ &= t\Psi(v). \end{aligned}$$

Combining the two inequalities, we find

$$\Phi(tv + (1-t)u^*) - \Phi(u^*) \leq t\Psi(v) + O(t^2),$$

so that indeed, for t small enough, $\Phi(tv + (1-t)u^*) < \Phi(u^*)$, leading to the announced contradiction.

Therefore, Ψ is nonnegative, which means that

$$\frac{1}{2\tau} \|u - u^*\|^2 \leq \Phi(u) - \Phi(u^*)$$

for all $u \in H$. \square

For a proper (i.e. not everywhere equal to ∞), lower semicontinuous, convex functional F , and $\tau > 0$, define the operator $J_\tau^F : H \rightarrow H$ by

$$J_\tau^F[u_0] := \operatorname{argmin}_{u \in H} \left(\frac{1}{2\tau} \|u - u_0\|^2 + F(u) \right).$$

Proposition 1 Let $F, G : H \rightarrow [0, \infty]$ be two non-negative, proper, lower semicontinuous, convex functionals on a Hilbert space H , such that for all $u \in H$,

$$F(u) - \delta \leq G(u) \leq F(u) + \delta. \quad (46)$$

Let $u_0, v_0 \in H$, such that

$$|\partial F|(u_0) \leq L \quad \text{and} \quad |\partial G|(v_0) \leq L. \quad (47)$$

Then, we have the following estimate for the gradient flow $u : [0, \infty) \rightarrow H$ of F starting at u_0 and the gradient flow $v : [0, \infty) \rightarrow H$ of G starting at v_0 :

$$\|u(t) - v(t)\| \leq \begin{cases} 4\sqrt{\delta t} + \|u_0 - v_0\| & \text{for } 0 \leq t \leq \frac{\delta}{L^2} \\ 8\sqrt[3]{L\delta t^2} + \|u_0 - v_0\| & \text{for } t > \frac{\delta}{L^2}. \end{cases}$$

The idea is that the stability estimate in Lemma 2 will allow us to conclude that $J_\tau^F[u_0]$ and $J_\tau^G[v_0]$ are close when u_0 and v_0 are close. By iterating the operators J_τ^F and J_τ^G , we approximate the gradient flows of F and G respectively, and from the slope estimate (54) we will derive that this approximation is uniform. This will allow us to derive bounds for the gradient flows from the bounds for J_τ^F and J_τ^G . We provide the proof in appendix B.

We now know that the gradient flows of F and G are close when the slopes $|\partial F|(u_0)$ and $|\partial G|(v_0)$ are bounded. This assumption can be rather stringent. We will relax it, and merely require that $F(u_0)$ and $G(v_0)$ are bounded by some constant $E > 0$, in exchange for a bound between gradient flows that is slightly worse. Our approach will be to run the gradient flow for a small time s from u_0 and v_0 , and use the regularizing property of the gradient flow to conclude a slope bound. On the other hand, if s is small, $u(s)$ and $v(s)$ will be close to u_0 and v_0 . We will then choose s (almost) optimally to derive a bound between the gradient flows.

4.2 Strong \mathbb{L}_2 -convergence of TV-flows

Theorem 1 *Let $F : H \rightarrow [0, \infty]$ and $G : H \rightarrow [0, \infty]$ be two proper, lower semicontinuous, convex functionals on a Hilbert space H , such that*

$$F(u) - \delta \leq G(u) \leq F(u) + \delta$$

for all $u \in H$. Let $u_0, v_0 \in H$ be such that $F(u_0) \leq E$ and $G(v_0) \leq E$ and $\|u_0 - u^*\| \leq M$ and $\|v_0 - v^*\| \leq M$, for some constants $E, M > 0$, where u^* and v^* minimize F and G respectively. The gradient flow $u : [0, \infty) \rightarrow H$ of F starting at u_0 , and the gradient flow $v : [0, \infty) \rightarrow H$ of G starting at v_0 satisfy

$$\|u(t) - v(t)\| \leq 16(ME\delta t^2)^{1/5} + \|u_0 - v_0\|$$

for all $0 \leq t < E^6 M^6 / \delta^9$.

Proof By the Evolution Variational Inequality [4, Theorem 4.0.4, (iii)], we know that for all $s > 0$

$$\|u(s) - u_0\| \leq \sqrt{2sF(u_0)} \quad (48a)$$

and

$$\|v(s) - v_0\| \leq \sqrt{2sG(v_0)}. \quad (48b)$$

By the regularizing property [4, Theorem 4.0.4, (ii)],

$$|\partial F|(u(s)) \leq \frac{1}{s} \|u_0 - u^*\| \leq \frac{M}{s} \quad (49a)$$

and

$$|\partial G|(v(s)) \leq \frac{1}{s} \|v_0 - v^*\| \leq \frac{M}{s} \quad (49b)$$

where u^* minimizes F and v^* minimizes G .

Because the gradient flow is a non-expansive semigroup [4, Theorem 4.0.4, (iv)], we get

$$\begin{aligned} \|u(t) - v(t)\| &\leq \|u(t+s) - v(t+s)\| + \|u(t+s) - u(t)\| \\ &\quad + \|v(t+s) - v(t)\| \\ &\leq \|u(t+s) - v(t+s)\| + \|u(s) - u_0\| \\ &\quad + \|v(s) - v_0\|. \end{aligned}$$

Now assume $t < E^6 M^6 / \delta^9$. We will want to choose s (almost) optimally, depending on t . We choose

$$s = \frac{M^{2/5} \delta^{2/5} t^{4/5}}{E^{3/5}}$$

and note that with $L := M/s$, we have

$$t \geq \frac{\delta}{L^2}.$$

By the slope estimates (49) we can apply Proposition 1 to the gradient flows starting at $u(s)$ and $v(s)$, to get

$$\begin{aligned} \|u(t) - v(t)\| &\leq 8M^{1/3} s^{-1/3} \delta^{1/3} t^{2/3} + \|u(s) - v(s)\| \\ &\quad + \|u(s) - u_0\| + \|v(s) - v_0\| \\ &\leq 8M^{1/3} s^{-1/3} \delta^{1/3} t^{2/3} + 2\|u(s) - u_0\| \\ &\quad + 2\|v(s) - v_0\| + \|u_0 - v_0\| \\ &\stackrel{(48)}{\leq} 8M^{1/3} s^{-1/3} \delta^{1/3} t^{2/3} + \sqrt{32sE} + \|u_0 - v_0\| \\ &= 16M^{1/5} \delta^{1/5} t^{2/5} E^{1/5} + \|u_0 - v_0\|. \end{aligned}$$

□

If, for the general result of Theorem 1, we take $F = TV_0$, $G = TV_\varepsilon$ and $\delta = \varepsilon |\Omega|$ we get the following result.

Corollary 1 (Strong \mathbb{L}_2 -convergence, stability and accuracy of TV-flows) *Let $U \in \mathbb{L}_2(\Omega)$ and let W^ε be the gradient flow of TV_ε starting at U and $\varepsilon, \epsilon \geq 0$. Let $t \geq 0$. Then*

$$\lim_{\varepsilon \downarrow 0} W^\varepsilon(\cdot, t) = W^0(\cdot, t) \quad \text{in } \mathbb{L}_2(\Omega).$$

More precisely, for $U \in BV(\Omega)$, we have for all $t \geq 0$:

$$\|W^\varepsilon(\cdot, t) - W^0(\cdot, t)\|_{\mathbb{L}_2(\Omega)} \leq 8 \left(\|U\|_{\mathbb{L}_2(\Omega)} (TV_0(U) + \delta) \delta t^2 \right)^{\frac{1}{5}}$$

with $\delta = \varepsilon |\Omega|$.

5 Experiments

In our experiments, we aim to enhance contour and fiber trajectories in medical images and to remove noise. Lifting the image $f : \mathbb{R}^d \rightarrow \mathbb{R}$ towards its orientation lift $U : \mathbb{M}_d \rightarrow \mathbb{R}$ defined on the space of positions and orientations $\mathbb{M} = \mathbb{R}^d \times S^{d-1}$ preserves crossings [24] and avoids leakage of wavefronts [21].

For our experiments for $d = 3$ the initial condition $U : \mathbb{M}_3 \rightarrow \mathbb{R}^+$ is a fiber orientation density function (FODF) obtained from DW-MRI data [32].

For our experiments for $d = 2$ the initial condition U is an invertible orientation score (OS).

For both $d = 2$ (Subsection 5.1) and $d = 3$ (Subsection 5.4), we show advantages of TVF and MCF over crossing-preserving diffusion flows [24, 15] on \mathbb{M}_d .

Finally, we include denoising experiments where we show qualitative and quantitative results where comparison with the well-known denoising technique BM3D[42] show advantages and good results.

5.1 Image Enhancement/Denoising

In accordance with the workflow in Fig. 1 we go through the following steps:

$$f \mapsto \mathcal{W}_\psi f \mapsto \Phi_t \circ \mathcal{W}_\psi f \mapsto f_t^a := \mathcal{W}_\psi^* \circ \Phi_t \circ \mathcal{W}_\psi f \quad (50)$$

$$\approx \int_{S^1} \Phi_t(\mathcal{W}_\psi f)(\cdot, \mathbf{n}) d\mu_{S^1}(\mathbf{n}).$$

for $t \geq 0$. With respect to the final step we recall that we use cake wavelets that allow for sharp approximate reconstruction by integration over angles only. Here $U \mapsto W(\cdot, t) = \Phi_t(U)$ denotes the flow operator on \mathbb{M}_2 (44). Hence the initial condition for our TVF/MCF-PDE (44) is set by an orientation score of image $f : \mathbb{R}^2 \rightarrow \mathbb{R}$ given by (2).

By the invertibility of the orientation score one has $f = f_0^a$ so all flows depart from the original image.

We refer to the different methods we experimented with with the following terms.

- MCF: we set $(a, b) = (1, 1)$.
- TVF: we set $(a, b) = (0, 1)$.
- Left invariant: we use the left invariant geometry per the first column of Table 1.
- Gauge: we use the locally adaptive frames geometry per the second column of Table 1.
- Isotropic: we set $\epsilon = 1$.
- Anisotropic: we set $\epsilon = 0.25$.
- With coherence enhancement: we use the PDE with the E operator per (44).

So that, for example, *Isotropic Gauge TVF with coherence enhancement* would equate to setting $(a, b) = (0, 1)$,

$\epsilon = 1$, includes the E operator in the PDE and uses the second column of Table 1 to define our geometrical objects.

For quantitative comparison we will look at relative \mathbb{L}_1 and \mathbb{L}_2 errors, meaning if we have a (clean) source image f_{source} and a denoised image f_t that has been processed to time t we calculate the relative error as:

$$\frac{\|f_t - f_{source}\|}{\|f_{source}\|}, \quad (51)$$

with the corresponding \mathbb{L}_1 or \mathbb{L}_2 norm.

We will test against two types of noise: Gaussian and correlated.

5.2 Gaussian noise.

We apply Gaussian noise with standard deviation 0.2 to our normalized (to $[0, 1]$) source image, the original and noisy images are shown in Fig. 8a respectively 8b.

In Fig. 5 we show how the errors progress with $t \geq 0$ for the isotropic ($\epsilon = 1$) case without coherence enhancement (i.e. without E). For comparison we plot the same error with spatial Perona-Malik. While Perona-Malik is clearly more stable and resilient to over-smoothing, both our proposed methods have much smaller minimal errors.

Remark 13 (Interpretation of timescales)

The different methods work on different timescales, we scale these to be able to plot the results together but no meaning should be attributed to one method obtaining a minimum earlier than another. The error graphs just show:

- how large the minimal error is and
- how fast the image deteriorates after this minimum has been reached.

Next we turn on anisotropy by setting $\epsilon = .25$, the resulting errors are plotted in Fig. 6. We gain no improvement in minimal error while needing more computational cycles to reach the minimum, from which we conclude that for this application isotropic processing is more desirable.

In Fig. 7 we show the errors for the isotropic setup with coherence enhancement turned on (for $c = .2$). We get a very minor improvement in minimal errors and a decent improvement in over-smoothing stability, although still not on the level of Perona-Malik. It is remarkable that with coherence enhancement turned on the data adaptive geometry is less stable than the left invariant geometry, we observe that combining two different methods of adapting to the data is counter-productive in this instance.

For a qualitative comparison of the different isotropic methods with coherence enhancement we over-smooth the collagen image past the time of its lowest \mathbb{L}_2 error with a factor of two, the corresponding qualitative results are shown in Fig. 8.

5.3 Correlated noise.

For correlated noise we apply a Gaussian filter with $\sigma = 1.0$ to Gaussian noise with $\sigma = 0.2$. The error evolution for the isotropic methods is plotted in Fig. 9. We observe that MCF performs worse in this setting against correlated noise, both in minimal error and stability it does not do as well as spatial Perona-Malik. TVF on the other hand has a better minimal error than Perona-Malik at the cost of stability, turning on the locally adaptive frames does improve stability somewhat.

The error evolution with coherence enhancement turned on is plotted in Fig. 10. Overall this improves the results but MCF still performs less good in this setting. TVF sees both an improvement in minimal error and stability. As with the Gaussian noise experiment we see that turning on both coherence enhancement and locally adaptive frames is counterproductive.

A qualitative comparison of the methods against correlated noise is shown in Fig. 11, where again we smooth twice the optimal time. We observe the same general trend as in Fig. 8, all methods do a good job of preserving edges but TVF stands out in clearing the plateaus.

As a final method to compare against we look at BM3D[42]. Both BM3D and our methods share a dependence on some prior knowledge for optimal performance: BM3D requires us to know the standard deviation of the noise and our method requires us to know the optimal processing time.

We make a qualitative comparison of removing correlated noise between BM3D and left invariant TVF by smoothing $1.5\times$ past the optimal \mathbb{L}_2 error: $1.5\times$ the optimal standard deviation in case of BM3D and $1.5\times$ the processing time in case of TVF. The resulting images are shown in Fig. 12.

For a broader comparison we compute peak-signal-to-noise-ratios for the collagen image we already saw and two additional images of different styles shown in Fig. 13. Results are summarized in Table 3.

As the gauge TVF method does well against correlated noise according to the PSNR value in Table 3 we will look at its qualitative result and compare it against BM3D in Fig. 14.

5.4 Denoising and Fiber Enhancement on FODFs in DW-MRI

In DW-MRI image processing one obtains a field of angular diffusivity profiles (orientation density function) of water-molecules. A high diffusivity in particular orientation correlates to biological fibers structure, in brain white matter, along that same direction. Crossing-preserving enhancement of FODF fields $U : \mathbb{M}_3 \rightarrow \mathbb{R}^+$ helps to better identify structural pathways in brain white matter, which is relevant for surgery planning, see for example [29, 32].

Gaussian noise	Collagen	Spiral	Mona Lisa
Noisy image	14.1	15.5	14.1
Perona-Malik	20.1	19.5	20.5
BM3D	23.1	21.4	23.9
Left inv. MCF	21.4	19.5	23.3
Gauge MCF	21.4	19.8	23.7
Left inv. TVF	22.9	20.9	26.0
Gauge TVF	22.9	21.2	26.1
Correlated noise	Collagen	Spiral	Mona Lisa
Noisy image	23.9	25.3	23.9
Perona-Malik	24.3	25.3	25.1
BM3D	24.0	21.4	26.3
Left inv. MCF	23.8	24.3	26.2
Gauge MCF	23.8	24.2	26.2
Left inv. TVF	24.8	25.7	26.8
Gauge TVF	24.9	25.9	26.9

Table 3: Comparing Peak-Signal-to-Noise-Ratio (dB) for the coherence enhanced methods against BM3D and spatial Perona-Malik at the minimal \mathbb{L}_2 error. Three images were tested, the first being the collagen image we have been using, second a spiral test image and third a grayscale Mona Lisa. Note that all these measurements depend on some ground-truth knowledge, knowing the standard deviation of the noise in the case of BM3D and knowing the optimal processing time in case of the others.

For a quantitative comparison we applied TVF, MCF and PM diffusion [15] to denoise a popular synthetic FODF $U : \mathbb{M}_3 \rightarrow \mathbb{R}^+$ from the Tractometer challenge with realistic noise profiles [16]. In Fig. 15, we can observe the many crossing fibers in the dataset. Furthermore, we depicted the absolute \mathbb{L}_2 -error $t \mapsto \|U - \Phi_t(U)\|_{\mathbb{L}_2(\mathbb{M}_3)}$ as a function of the evolution parameter t , where $\Phi_t(U) = W_\varepsilon(\cdot, t)$ with optimized $\varepsilon = 0.02$ in the case of TVF (in green), and MCF (in blue), and where Φ_t is the PM diffusion evolution [15] on \mathbb{M}_3 with optimized PM parameter $K = 0.2$ (in red). We also depict results for $K = 0.1, 0.4$ (with the dashed lines) and $\varepsilon = 0.01, 0.04$. We see that the other parameter settings provide on average worse results, justifying our optimized parameter settings. We set $D_S = 1.0, D_A = 0.001, \Delta t = 0.01$. We observe that:

- TVF can reach lower error values than MC-flow with adequate $\Delta t = 0.01$,
- MCF provides more stable errors for all $t > 0$, than TV-flow w.r.t. $\varepsilon > 0$,
- TVF and MCF produce lower error values than PM-diffusion,
- PM-diffusion provides the most variable results for all $t > 0$.

For a qualitative comparison we applied TVF, MCF, PM diffusion and linear diffusion to a FODF field $U : \mathbb{M}_3 \rightarrow \mathbb{R}^+$ obtained from a standard DW-MRI dataset (with $b =$

1000s/mm², 54 gradient directions) via constrained spherical deconvolution (CSD) [37]. See Fig. 16, where for each method, we used the optimal parameter settings with the artificial data-set. We see that

- all methods perform well on the real datasets. Contextual alignment of the angular profiles better reflects the anatomical fiber bundles,
- MCF and TVF better preserve boundaries and angular sharpness,
- MCF better preserves the amplitude at crossings at longer times.

6 Conclusion

We have proposed a PDE system on the homogeneous space $\mathbb{M}_d = \mathbb{R}^d \times S^{d-1}$ of positions and orientations, for crossing-preserving denoising and enhancement of (lifted) images containing both complex elongated structures and plateaus.

It includes TVF, MCF and diffusion flows as special cases, and includes (sub-)Riemannian geometry. Thereby we generalized recent related works by Citti et al. [12] and Chambolle & Pock [11] from 2D to 3D using a different numerical scheme with new convergence results (Theorem 1) and stability bounds. We used the divergence and intrinsic gradient on a (sub-)Riemannian manifold above \mathbb{M}_d for a formal weak-formulation of total variation flows, which simplifies if the lifted images are differentiable (Lemma 1).

For 2D image denoising and enhancement we have shown that in all cases TVF on \mathbb{M}_2 has a better minimal error than Perona-Malik and MCF at the cost of being more sensitive to oversmoothing, recall Fig. 5 to 11. The \mathbb{L}_1 , \mathbb{L}_2 and PSNR measures indicate the potential of our proposed methods for denoising and we manage to improve PSNR results against methods such as BM3D against correlated noise on some images, recall Fig. 12 & 14. Qualitatively this is mainly reflected in better clearing of plateaus while still preserving hard edges and crossings.

In 3D we compared to previous nonlinear crossing-preserving diffusion methods on \mathbb{M}_3 , we showed improvements over Perona-Malik and improvements over contextual fiber enhancement methods in DW-MRI processing [15, 18] on real medical image data. We observe that crossings and boundaries (of bundles and plateaus) are better preserved over time. We support this quantitatively by a denoising experiment on a benchmark DW-MRI dataset, where MCF performs better than TVF and both perform better than Perona-Malik diffusions, in view of error reduction and stability.

Altogether, we conclude that our TVF and MCF methods on \mathbb{M}_d work well for denoising and enhancement for both $d = 2$ and $d = 3$. In general we see clear benefits of the inclusion of locally adaptive frames and of limited inclusion of coherence enhancement. The code from

our experiments is available as a Mathematica notebook at https://bmsmets.com/files/tvf_mcf_denoising_jmiv.nb

Future work. While we have shown the potential of our PDE system on \mathbb{M}_d as a denoising/enhancement method some challenges remain for future work:

- Determining stopping time; our methods show good minimal errors but are prone to degrading the image if left running for too long. For general applications a robust automatic stopping method would be required. Spectral analysis of nonlinear operators[44, 45] could be of help here.
- Coherence enhancement [39] was not originally conceived for denoising even though it has been evaluated for that purpose [20]. It should be evaluated how a purpose designed method such as Improved Edge Enhancing Diffusion[46] (IEED) performs when generalized to \mathbb{M}_d , i.e. we would reformulate our enhancement operator E as:

$$E := \int_{S^d} \mathbf{c} \otimes \mathbf{c} e^{\frac{|\nabla U \cdot \mathbf{c}|^2}{2\kappa^2}} d\mu(\mathbf{c}),$$

and test its performance.

Appendix A Left Invariant Vector Field Basis for $SE(3)$

Two charts are required to cover $SO(3)$, when using ZYZ-Euler angles:

$$g = \left(x, y, z, R_{\mathbf{e}_z, \gamma} R_{\mathbf{e}_y, \beta} R_{\mathbf{e}_z, \alpha} \right), \quad (52)$$

where $\beta \in (0, \pi)$ and $\alpha, \gamma \in [0, 2\pi)$, the left invariant vector field basis is given by:

$$\mathcal{A}_1|_g = (\cos \alpha \cos \beta \cos \gamma - \sin \alpha \sin \gamma) \partial_x + (\sin \alpha \cos \beta \cos \gamma + \cos \alpha \sin \gamma) \partial_y - \cos \alpha \sin \beta \partial_z,$$

$$\mathcal{A}_2|_g = (-\sin \alpha \cos \beta \cos \gamma - \cos \alpha \sin \gamma) \partial_x + (\cos \alpha \cos \beta \cos \gamma - \sin \alpha \sin \gamma) \partial_y + \sin \alpha \sin \beta \partial_z,$$

$$\mathcal{A}_3|_g = \sin \beta \cos \gamma \partial_x + \sin \beta \sin \gamma \partial_y + \cos \beta \partial_z,$$

$$\mathcal{A}_4|_g = \cos \alpha \cot \beta \partial_\alpha + \sin \alpha \partial_\beta - \frac{\cos \alpha}{\sin \beta} \partial_\gamma,$$

$$\mathcal{A}_5|_g = -\sin \alpha \cot \beta \partial_\alpha + \cos \alpha \partial_\beta + \frac{\sin \alpha}{\sin \beta} \partial_\gamma,$$

$$\mathcal{A}_6|_g = \partial_\alpha.$$

The above set of expressions are not valid for $\beta = 0$ or $\beta = \pi$, in that case we can switch to XYZ-Euler angles:

$$g = \left(x, y, z, R_{\mathbf{e}_z, \gamma'} R_{\mathbf{e}_y, \beta'} R_{\mathbf{e}_x, \alpha'} \right), \quad (53)$$

with $\alpha' \in [0, 2\pi)$, $\beta' \in [-\pi, \pi)$ and $\gamma' \in (-\pi/2, \pi/2)$. The basis vector fields are then given by:

$$\begin{aligned} \mathcal{A}_1|_g &= \cos \alpha' \cos \beta' \partial_x + (\cos \gamma' \sin \alpha' + \cos \alpha' \sin \beta' \sin \gamma') \partial_y \\ &\quad + (\sin \alpha' \sin \gamma' - \cos \alpha' \sin \beta' \cos \gamma') \partial_z, \\ \mathcal{A}_2|_g &= -\sin \alpha' \cos \beta' \partial_x + (\cos \alpha' \cos \gamma' - \sin \alpha' \sin \beta' \sin \gamma') \partial_y \\ &\quad + (\sin \alpha' \sin \beta' \cos \gamma' + \cos \alpha' \sin \gamma') \partial_z, \\ \mathcal{A}_3|_g &= \sin \beta' \partial_x - \cos \beta' \sin \gamma' \partial_y + \cos \beta' \cos \gamma' \partial_z, \end{aligned}$$

$$\mathcal{A}_4|_g = -\cos \alpha' \tan \beta' \partial_{\alpha'} + \sin \alpha' \partial_{\beta'} + \frac{\cos \alpha'}{\cos \beta'} \partial_{\gamma'},$$

$$\mathcal{A}_5|_g = \sin \alpha' \tan \beta' \partial_{\alpha'} + \cos \alpha' \partial_{\beta'} - \frac{\sin \alpha'}{\cos \beta'} \partial_{\gamma'},$$

$$\mathcal{A}_6|_g = \partial_{\alpha'},$$

for $|\beta'| \neq \pi/2$.

Appendix B Proof of Proposition 1

We recall the proposition and give a proof.

Proposition 1 *Let $F, G : H \rightarrow [0, \infty]$ be two non-negative, proper, lower semicontinuous, convex functionals on a Hilbert space H , such that for all $u \in H$,*

$$F(u) - \delta \leq G(u) \leq F(u) + \delta. \quad (54)$$

Let $u_0, v_0 \in H$, such that

$$|\partial F|(u_0) \leq L \quad \text{and} \quad |\partial G|(v_0) \leq L. \quad (55)$$

Then, we have the following estimate for the gradient flow $u : [0, \infty) \rightarrow H$ of F starting at u_0 and the gradient flow $v : [0, \infty) \rightarrow H$ of G starting at v_0 :

$$\|u(t) - v(t)\| \leq \begin{cases} 4\sqrt{\delta t} + \|u_0 - v_0\| & \text{for } 0 \leq t \leq \frac{\delta}{L^2} \\ 8\sqrt[3]{L\delta t^2} + \|u_0 - v_0\| & \text{for } t > \frac{\delta}{L^2}. \end{cases}$$

Proof Let $\tau > 0$ and let $u_1^F := J_\tau^F[u_0]$ and $v_1^G := J_\tau^G[v_0]$. Set also $v_1^F := J_\tau^F[v_0]$ and $u_1^G := J_\tau^G[u_0]$. Then, using the definition of v_1^F in the second inequality below, we find

$$\begin{aligned} &\frac{1}{2\tau} \|v_1^F - v_0\|^2 + G(v_1^F) \\ &\stackrel{(54)}{\leq} \frac{1}{2\tau} \|v_1^F - v_0\|^2 + F(v_1^F) + \delta \\ &\leq \frac{1}{2\tau} \|v_1^G - v_0\|^2 + F(v_1^G) + \delta \\ &\stackrel{(54)}{\leq} \frac{1}{2\tau} \|v_1^G - v_0\|^2 + G(v_1^G) + 2\delta. \end{aligned}$$

Because the functional

$$v \mapsto \frac{1}{2\tau} \|v - v_0\|^2 + G(v)$$

is $1/\tau$ -convex, it follows by Lemma 2 that

$$\frac{1}{2\tau} \|v_1^F - v_1^G\|^2 \leq 2\delta.$$

Now we use that J_τ^F is non-expansive [4, Eq. (4.0.2)], so

$$\|u_1^F - v_1^F\| = \|J_\tau^F(u_0) - J_\tau^F(v_0)\| \leq \|u_0 - v_0\|.$$

We conclude that

$$\|u_1^F - v_1^G\| \leq \|u_0 - v_0\| + 2\sqrt{\delta\tau}.$$

By iterating this estimate, we derive

$$\|(J_\tau^F)^n[u_0] - (J_\tau^G)^n[v_0]\| \leq \|u_0 - v_0\| + 2n\sqrt{\delta\tau}. \quad (56)$$

The a priori estimate [4, Theorem 4.0.4, (v)] yields that the gradient flows u and v of F and G respectively are approximated well by $(J_{t/n}^F)^n[u_0]$ and $(J_{t/n}^G)^n[v_0]$. More precisely, for $t > 0$ and $n > 0$, the a priori estimate gives

$$\|u(t) - (J_\tau^F)^n\| \leq \frac{Lt}{\sqrt{2n}} \quad \text{and} \quad \|v(t) - (J_\tau^G)^n\| \leq \frac{Lt}{\sqrt{2n}}.$$

By these a priori estimates and the estimate for the discrete flows (56), we see that

$$\begin{aligned} \|u(t) - v(t)\| &\leq \|u(t) - (J_{t/n}^F)^n[u_0]\| + \|v(t) - (J_{t/n}^G)^n[v_0]\| \\ &\quad + \|(J_{t/n}^F)^n[u_0] - (J_{t/n}^G)^n[v_0]\| \\ &\leq \sqrt{2L} \frac{t}{n} + 2n\sqrt{\frac{\delta t}{n}} + \|u_0 - v_0\|. \end{aligned}$$

To derive the final estimates, we need to make good choices for n . If $0 \leq t \leq \delta/L^2$, we take $n = 1$ and obtain

$$\begin{aligned} \|u(t) - v(t)\| &\leq \sqrt{2L}t + 2\sqrt{\delta t} + \|u_0 - v_0\| \\ &\leq 4\sqrt{\delta t} + \|u_0 - v_0\|. \end{aligned}$$

If $t > \delta/L^2$, we choose $n = \lceil L^{2/3}(t/\delta)^{1/3} \rceil$, which is larger than or equal to 2. In that case,

$$n/2 \leq n-1 < L^{2/3}(t/\delta)^{1/3} \leq n.$$

We then obtain

$$\|u(t) - v(t)\| \leq 8L^{1/3}\delta^{1/3}t^{2/3} + \|u_0 - v_0\|.$$

□

References

1. Duits, R., St-Onge, E., Portegies, J., Smets, B.: Total Variation and Mean Curvature PDEs on the Space of Positions and Orientations. *International Conference on Scale Space and Variational Methods in Computer Vision*, 211–223 (2019)
2. Ghimpeanu, G., Batard, T., Bertalmo, M., Levine, S. (2015). A decomposition framework for image denoising algorithms. *IEEE transactions on image processing*, 25(1), 388–399.
3. Bertalmo, M., Calatroni, L., Franceschi, V., Franceschiello, B., Prandi, D. (2019, June). A cortical-inspired model for orientation-dependent contrast perception: a link with Wilson-Cowan equations. In *International Conference on Scale Space and Variational Methods in Computer Vision* (pp. 472–484). Springer, Cham.
4. Ambrosio, L., Gigli, N., Savaré, G.: *Gradient flows in metric spaces and in the space of probability measures*. Birkhäuser (2005)
5. Baspinar, E., Citti, G., Sarti, A.: A geometric model of multi-scale orientation preference maps via gabor functions. *JMIV* **60**(6), 900–912 (2018)
6. Baspinar, E.: *Minimal Surfaces in Sub-Riemannian Structures and Functional Geometry of the Visual Cortex*. Ph.D. thesis, University of Bologna (2018)
7. Bekkers, E.: *Retinal Image Analysis using Sub-Riemannian Geometry in $SE(2)$* . Ph.D. thesis, TU/e Eindhoven (2017)
8. Bekkers, E., Duits, R., Mashatkov, A., Sanguinetti, G.: A PDE approach to data-driven sub-Riemannian geodesics in $SE(2)$. *SIIMS* **8**(4), 2740–2770 (2015)
9. Boscaïn, U., Chertovskih, R., Gauthier, J.P., Prandi, D., Remizov, A.: Highly corrupted image inpainting by hypoelliptic diffusion. *JMIV* **60**(8), 1231–1245 (2018)
10. Brézis, H.: *Opérateurs maximaux monotones et semi-grotes de contractions dans les espaces de Hilbert*, vol. 50. North-Holland Publishing Co. (1973)
11. Chambolle, A., Pock, T.: Total roto-translation variation. *Arxiv:17009.09953v2* pp. 1–47 (july 2018)
12. Citti, G., Franceschiello, B., Sanguinetti, G., Sarti, A.: Sub-riemannian mean curvature flow for image processing. *SIIMS* **9**(1), 212–237 (2016)
13. Citti, G., Sarti, A.: A cortical based model of perceptual completion in the roto-translation space. *JMIV* **24**(3), 307–326 (2006)
14. Cohen, E., Deffieux, T., Demené, C., Cohen, L., Tanter, M.: 3d vessel extraction in the rat brain from ultrasensitive doppler images. *Computer Methods in Biomechanics and Biomedical Engineering*. LNB pp. 81–91 (2018)
15. Creusen, E.J. & Duits, R., Florack, L., Vilanova, A.: Numerical schemes for linear and non-linear enhancement of DW-MRI. *NM-TMA* **6**(3), 138–168 (2013)
16. Neher, P.F., Laun, F.B., Stieltjes, B. and MaierHein, K.H.: Fiberfox: facilitating the creation of realistic white matter software phantoms. *Magnetic resonance in medicine* **72**(5), 1460–1470 (2014)
17. Duits, R.: *Perceptual organization in image analysis*. Ph.D. thesis, TU/e (2005)
18. Duits, R., Creusen, E., Ghosh, A., Dela Haije, T.: Morphological and linear scale spaces for fiber enhancement in DW-MRI. *JMIV* **46**(3), 326–368 (2013)
19. Duits, R., Franken, E.M.: Left invariant parabolic evolution equations on $SE(2)$ and contour enhancement via invertible orientation scores, part I: Linear left-invariant diffusion equations on $SE(2)$. *QAM-AMS* **68**, 255–292 (2010)
20. Duits, R., Janssen, M., Hannink, J., Sanguinetti, G.: Locally adaptive frames in the roto-translation group and their applications in medical image processing. *JMIV* **56**(3), 367–402 (2016)
21. Duits, R., Meesters, S., Mirebeau, J., Portegies, J.: Optimal paths for variants of the 2D and 3D Reeds-Shepp car with applications in image analysis. *JMIV* **60**, 816–848 (2018)
22. Evans, L.C., Spruck, J.: Motion of level sets by mean curvature. *I. J. Differential Geom.* **33**(3), 635–681 (1991)
23. Felsberg, M., Forssen, P.E., Schar, H.: Channel smoothing: Efficient robust smoothing of low-level signal features. *IEEE PAMI* pp. 209–222 (2006)
24. Franken, E.M., Duits, R.: Crossing preserving coherence-enhancing diffusion on invertible orientation scores. *IJCV* **85**(3), 253–278 (2009)
25. Giga, Y., Sato, M.H.: Generalized interface evolution with the Neumann boundary condition. *Proc. Japan Acad. Ser. A Math. Sci.* **67**(8), 263–266 (1991)
26. G.Sapiro: *Geometric Partial Differential Equations & Image Analysis*. CUP (2006)
27. Janssen, M.H.J., Janssen, A.J.E.M., Bekkers, E.J., Bescós, J.O., Duits, R.: Processing of invertible orientation scores of 3d images. *JMIV* **60**(9), 1427–1458 (2018)
28. Martin, F., Bekkers, E., Duits, R.: Lie analysis package: www.lieanalysis.nl/ (2017)
29. Meesters, S., et al.: Stability metrics for optic radiation tractography: Towards damage prediction after resective surgery. *Journal of Neuroscience Methods* (2017)
30. Perona, P., Malik, J. (1990). Scale-space and edge detection using anisotropic diffusion. *IEEE Transactions on pattern analysis and machine intelligence*, 12(7), 629–639.
31. Portegies, J.M., Duits, R.: New exact and numerical solutions of the (convection-) diffusion kernels on $SE(3)$. *DGA* **53**, 182–219 (2017)
32. Portegies, J.M., Fick, R., Sanguinetti, G.R., Meesters, S.P.L., Girard, G., Duits, R.: Improving Fiber Alignment in HARDI by Combining Contextual PDE Flow with Constrained Spherical Deconvolution. *PLoS ONE* **10**(10) (2015)
33. Portegies, J.: *PDEs on the Lie Group $SE(3)$ and their Applications in Diffusion-Weighted MRI*. Ph.D. thesis, Dep. Math. TU/e (2018)
34. Reiser, M., Burkhardt, H.: Efficient tensor voting with 3d tensorial harmonics. In: *CVPRW '08. IEEE Conf.* pp. 1–7 (2008)
35. Sato, M.H.: Interface evolution with Neumann boundary condition. *Adv. Math. Sci. Appl.* **4**(1), 249–264 (1994)
36. Schmidt, M., Weickert, J.: Morphological counterparts of linear shift-invariant scale-spaces. *Journal of Mathematical Imaging and Vision* **56**(2), 352–366 (2016)
37. Tournier, J.D., Calamante, F., Connelly, A.: MRtrix: Diffusion tractography in crossing fiber regions. *Int. J. Imag. Syst. Tech.* **22**(1), 53–66 (2012)
38. Vogt, T., Lellmann, J.: Measure-valued variational models with applications to diffusion-weighted imaging. *JMIV* **60**(9), 14821502 (2018)
39. Weickert, J.A.: Coherence-enhancing diffusion filtering **31**(2/3), 111–127 (1999)
40. Smets, B.M.N.: *Geometric Image Denoising and Machine Learning*. MSc. thesis, Dep. Math. TU/e (2019)
41. Franken, E.: *Enhancement of Crossing Elongated Structures in Images*. PhD thesis, Technical University Eindhoven (2008)
42. Dabov, K., Foi, A., Katkovnik, V., Egiazarian, K. (2007). Image denoising by sparse 3-D transform-domain collaborative filtering. *Image Processing*, *IEEE Transactions on* 16 (8), pp. 2080-2095.
43. Lebrun, M. (2012). An analysis and implementation of the BM3D image denoising method. *Image Processing On Line*, 2, 175-213.
44. Cohen, I., Falik, A., Gilboa, G. (2019, June). Stable Explicit p-Laplacian Flows Based on Nonlinear Eigenvalue Analysis. In *International Conference on Scale Space and Variational Methods in Computer Vision* (pp. 315-327). Springer, Cham.
45. Bungert, L., Burger, M., Tenbrinck, D. (2019, June). Computing nonlinear eigenfunctions via gradient flow extinction. In *International Conference on Scale Space and Variational Methods in Computer Vision* (pp. 291-302). Springer, Cham.
46. Fabbri, Luca, et al. Improved edge enhancing diffusion filter for speckle-corrupted images. *IEEE Geoscience and Remote Sensing Letters* 11.1 (2013): 99-103.

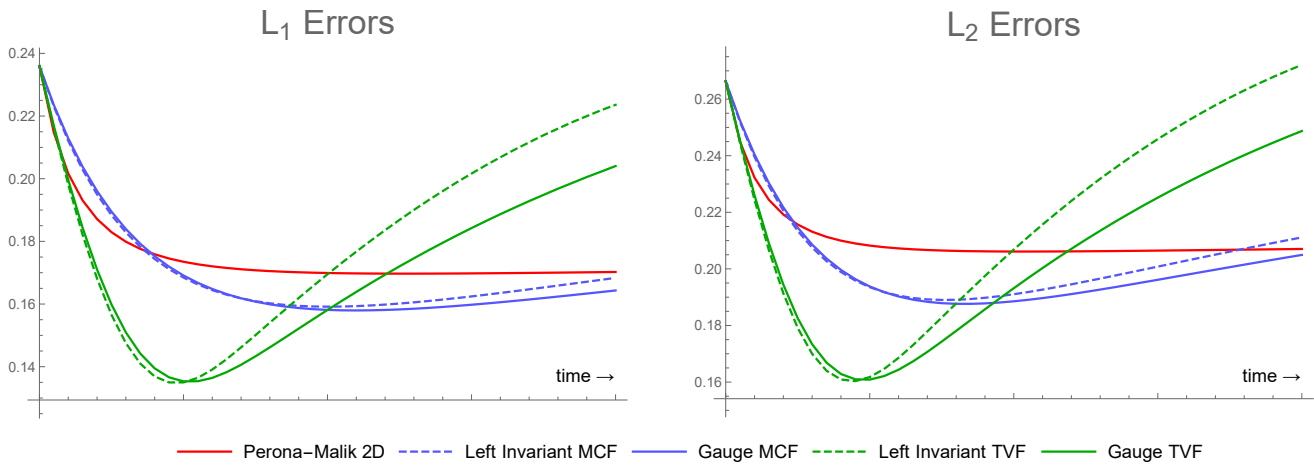


Fig. 5: Isotropic ($\epsilon = 1$) evolution of relative \mathbb{L}_1 and \mathbb{L}_2 errors over time of the collagen image with Gaussian noise benchmarked against spatial Perona-Malik. Remaining parameters are $D_S = 1$, $D_A = .01$ and $\epsilon = .001$.

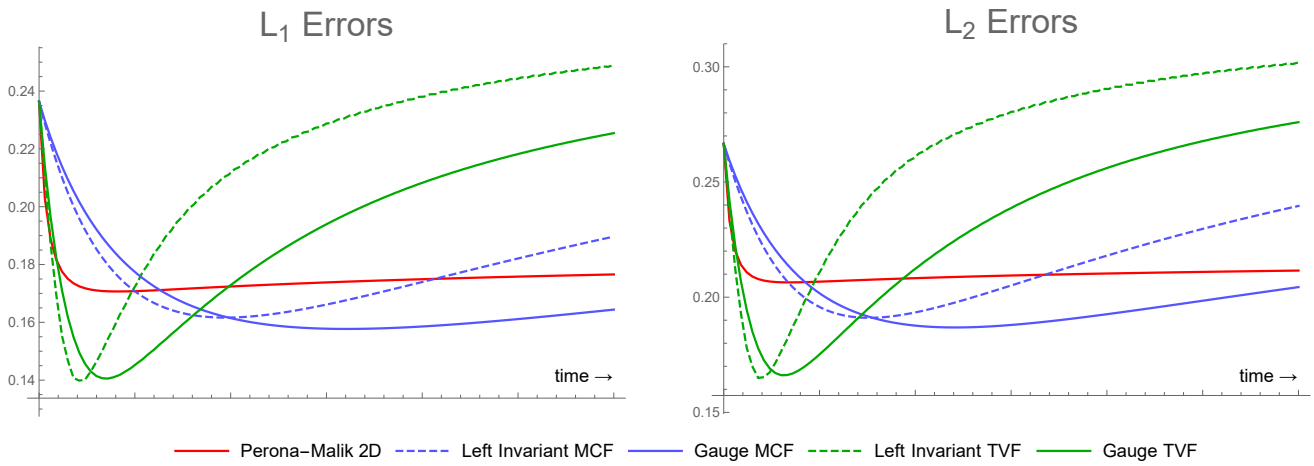


Fig. 6: Anisotropic ($\epsilon = .25$) evolution of relative \mathbb{L}_1 and \mathbb{L}_2 errors over time of the collagen image with Gaussian noise benchmarked against spatial Perona-Malik. Run with parameters $D_S = 1$, $D_A = .01$ and $\epsilon = .001$, note the much larger evolution time due to the smaller contribution of the lateral components. The resulting errors are slightly worse than the isotropic setup from Fig. 5.

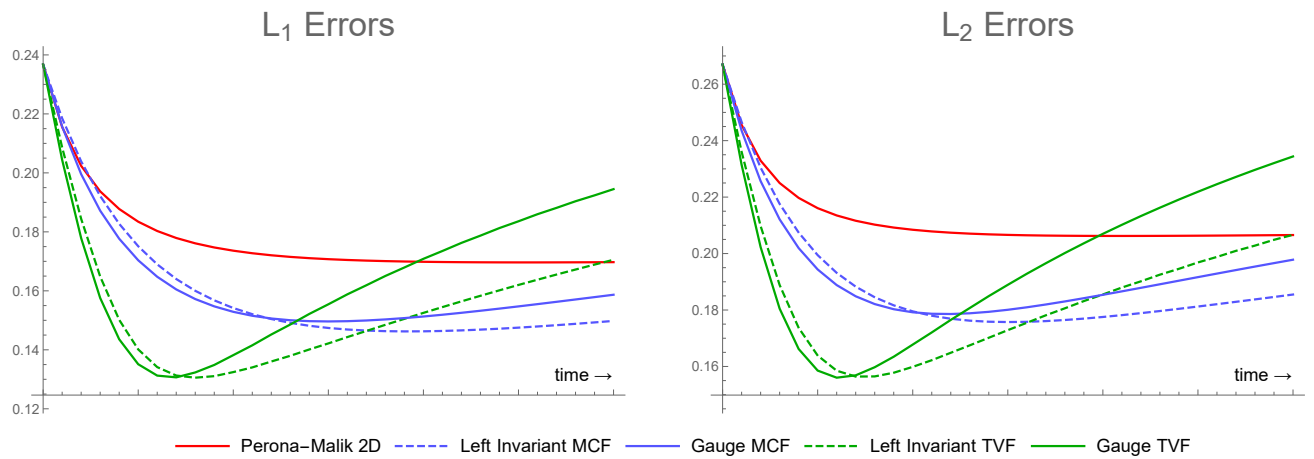


Fig. 7: Isotropic with coherence enhancement evolution of relative \mathbb{L}_1 and \mathbb{L}_2 errors over time of the collagen image with Gaussian noise benchmarked against spatial Perona-Malik. Run with parameters $D_S = 1$, $D_A = .01$, $\epsilon = .001$ and $c = .2$.

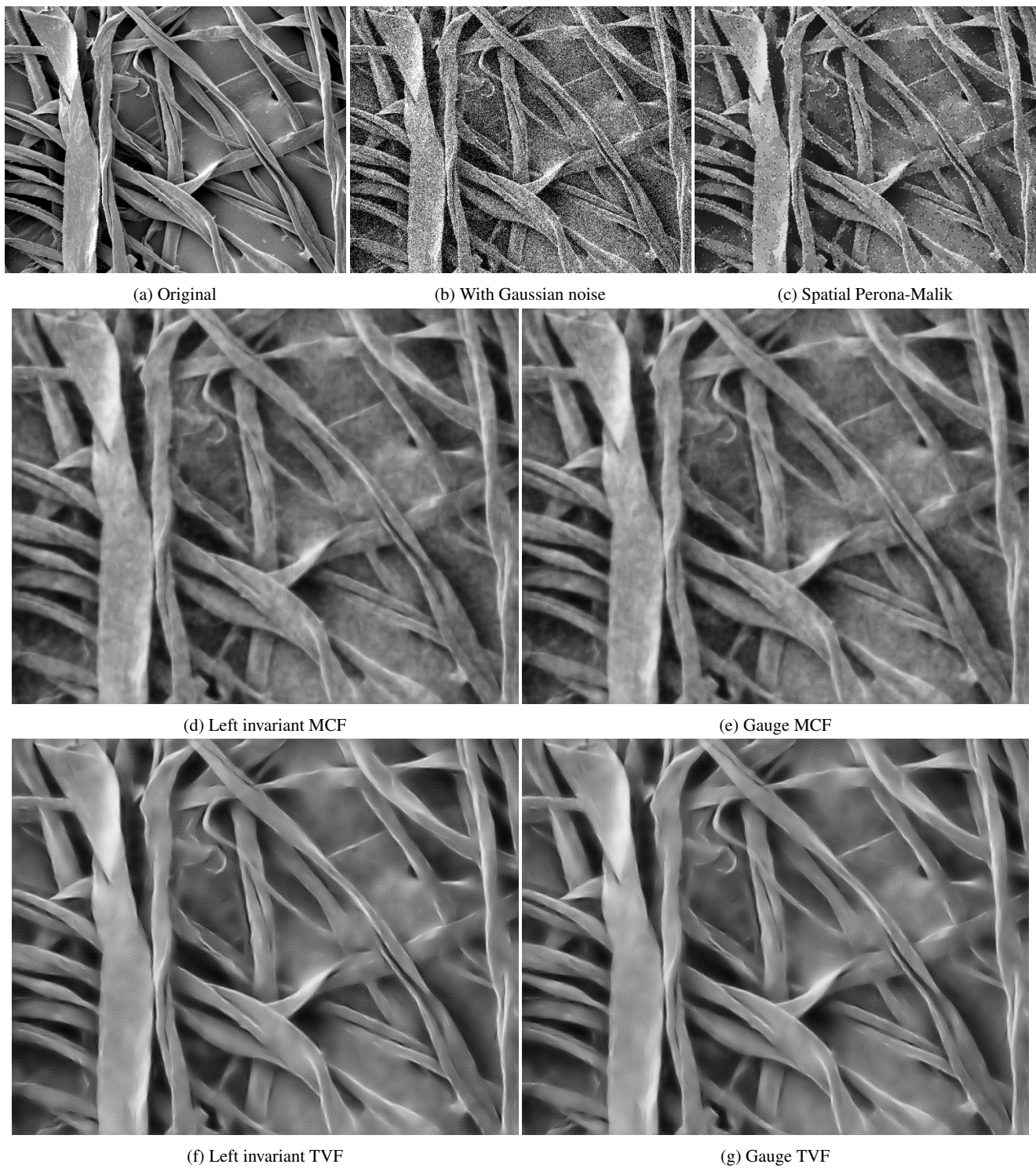


Fig. 8: Qualitative comparison of over-smoothed collagen images starting from a noisy image with $\sigma = .2$ Gaussian noise. Images are smoothed for twice the time needed to reach their minimal \mathbb{L}_2 error per Fig. 7. We use isotropic processing with coherence enhancement.

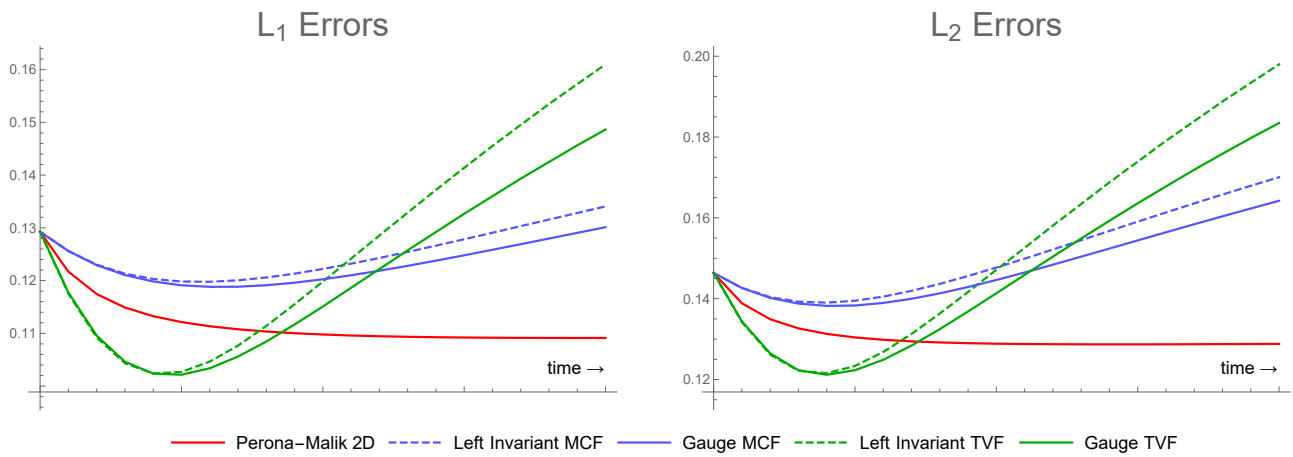


Fig. 9: Isotropic ($\epsilon = 1$) evolution of relative \mathbb{L}_1 and \mathbb{L}_2 errors over time of the collagen image with correlated noise ($\sigma = 0.2$ Gaussian noise with $r = 2$ and $\sigma = 1$ Gaussian Filter) benchmarked against spatial Perona-Malik. Remaining parameters are $D_S = 1$, $D_A = .01$ and $\epsilon = .001$.

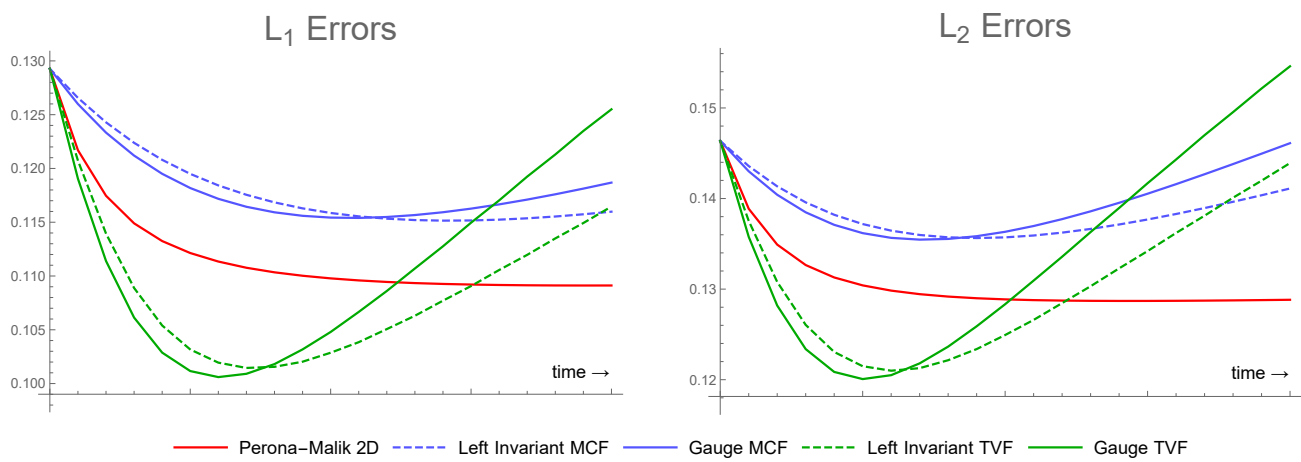


Fig. 10: Isotropic with coherence enhancement evolution of relative \mathbb{L}_1 and \mathbb{L}_2 errors over time of the collagen image with correlated noise ($\sigma = 0.2$ Gaussian noise with $r = 2$ Gaussian Filter) benchmarked against spatial Perona-Malik. Run with parameters $D_S = 1$, $D_A = .01$, $\epsilon = .001$ and $c = .2$.

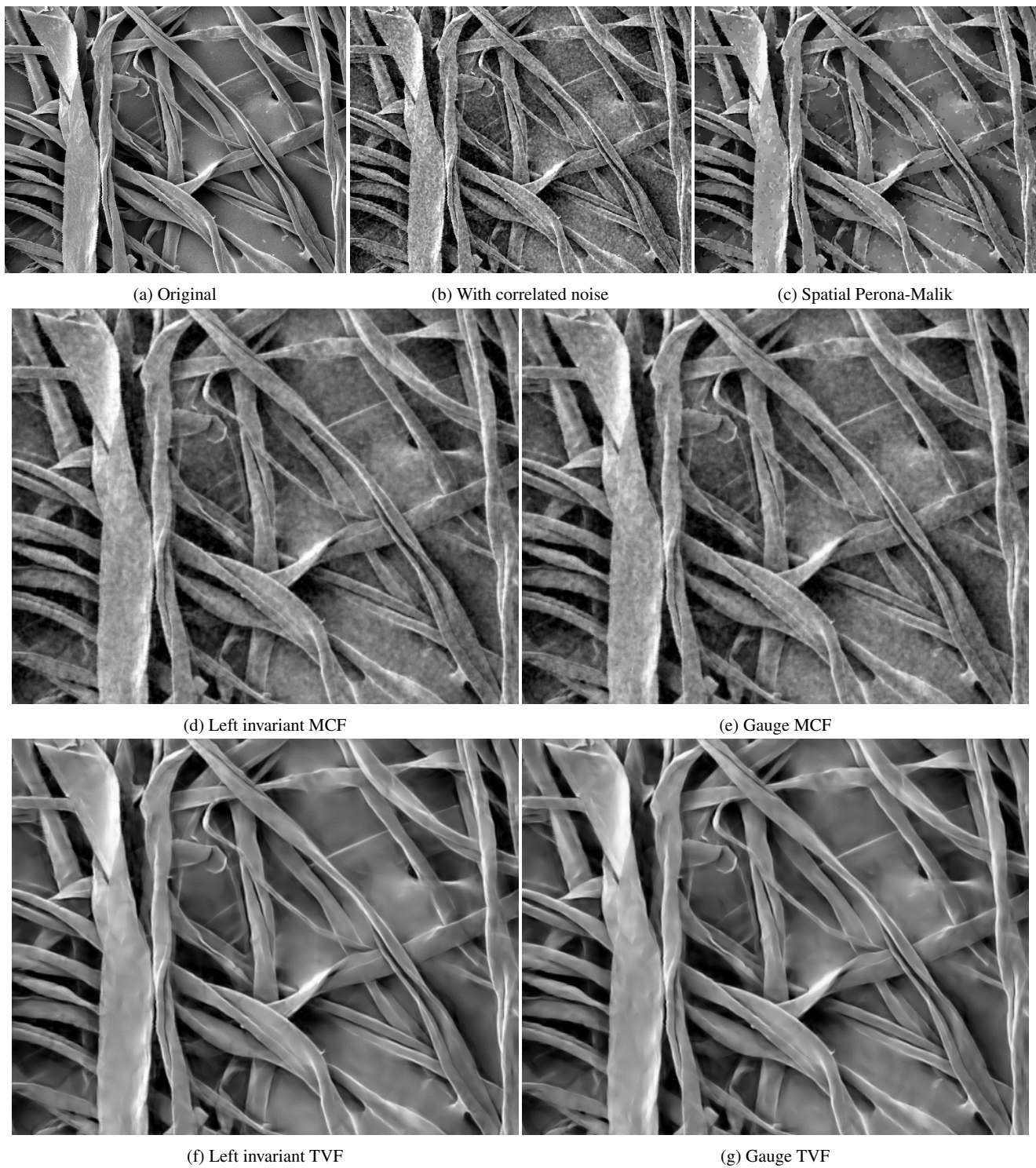


Fig. 11: Qualitative comparison of over-smoothed collagen images starting from a noisy image with correlated noise ($\sigma = 0.2$ Gaussian noise with $r = 2$ Gaussian Filter). Images are smoothed for twice the time needed to reach their minimal \mathbb{L}_2 error per Fig. 10. We use isotropic processing with coherence enhancement.

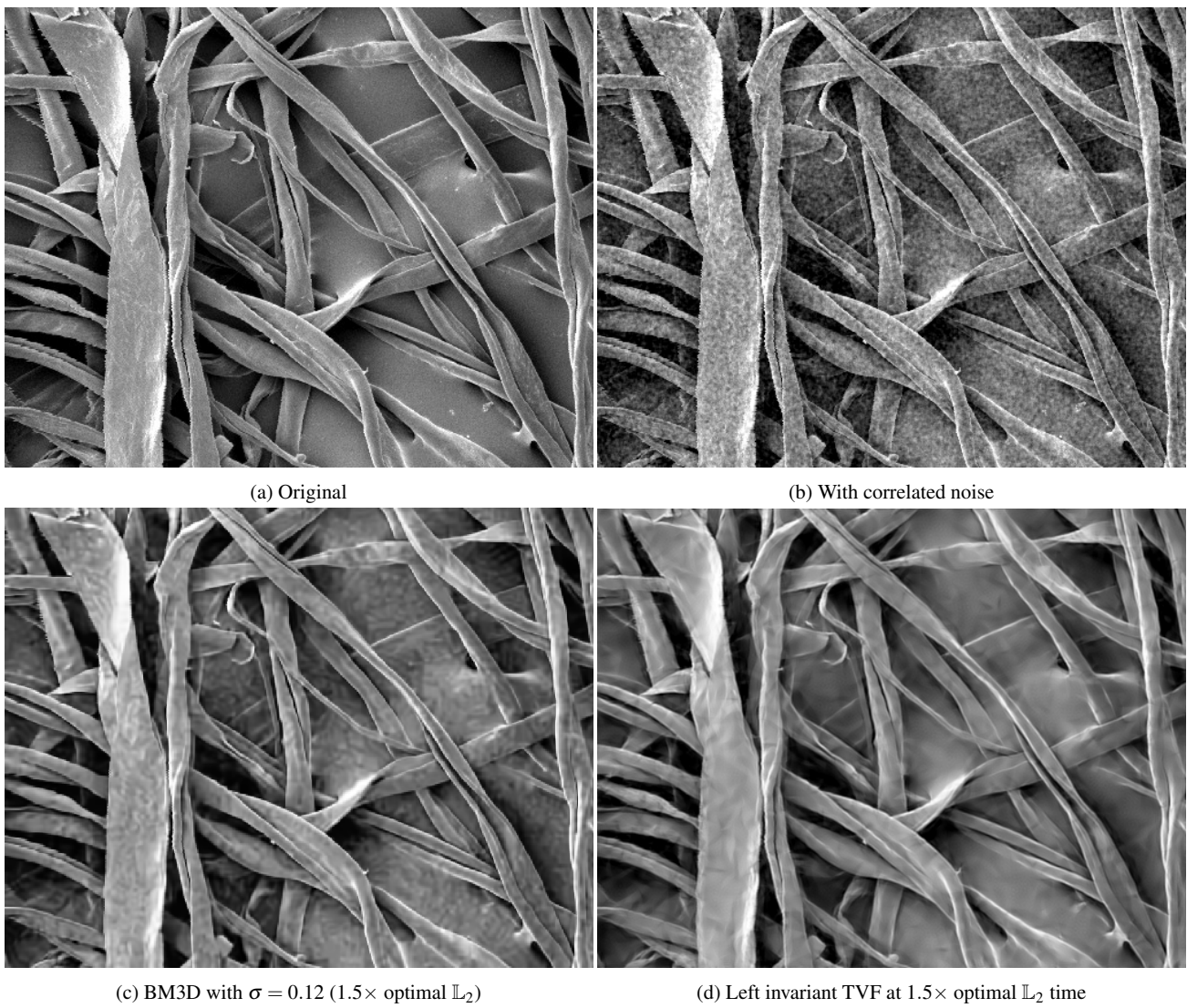


Fig. 12: Comparison of left invariant TVF with coherence enhancement against BM3D. Pay particular attention to the diagonal edges.



Fig. 13: A spiral test image and a monochrome Mona-Lisa that were used for the PSNR experiments in Table 3.

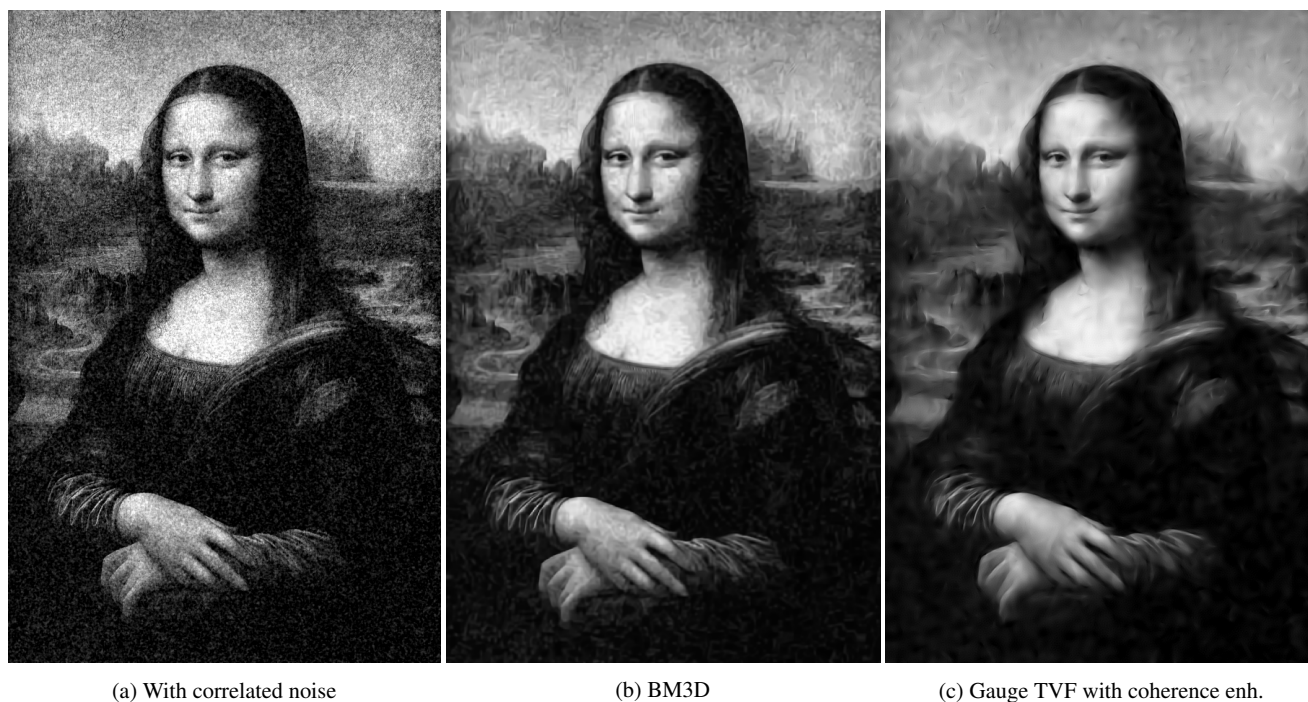


Fig. 14: Comparing Gauge TVF with coherence enhancement and BM3D against correlated noise, the standard deviation for BM3D and the evolution time for TVF were set at 1.5 times the number needed to reach the optimal \mathbb{L}_2 error.

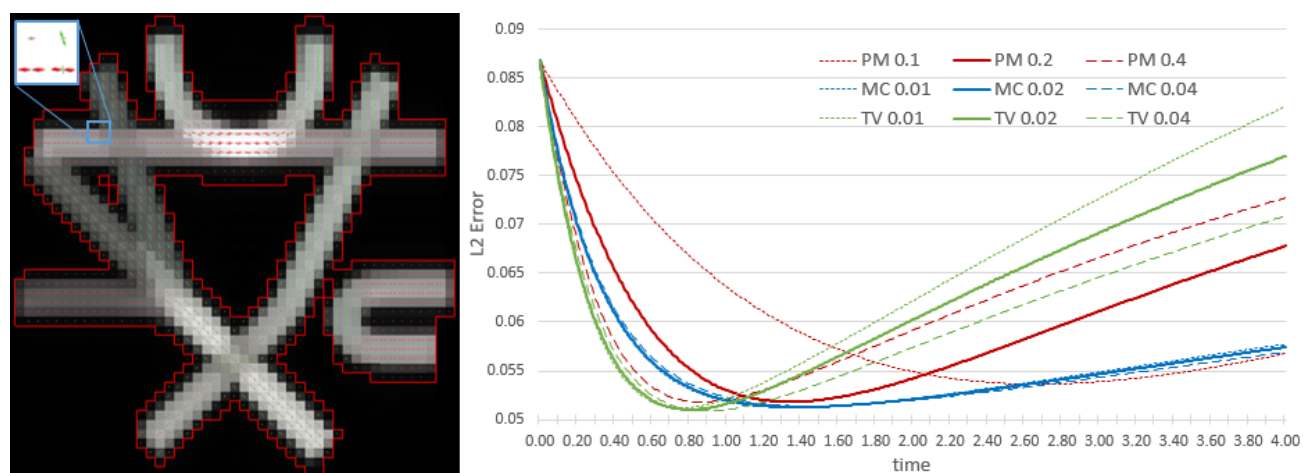


Fig. 15: Quantitative comparison of denoising a fiber orientation density function (FODF) obtained by (CSD) [37] from a benchmark DW-MRI dataset [16].

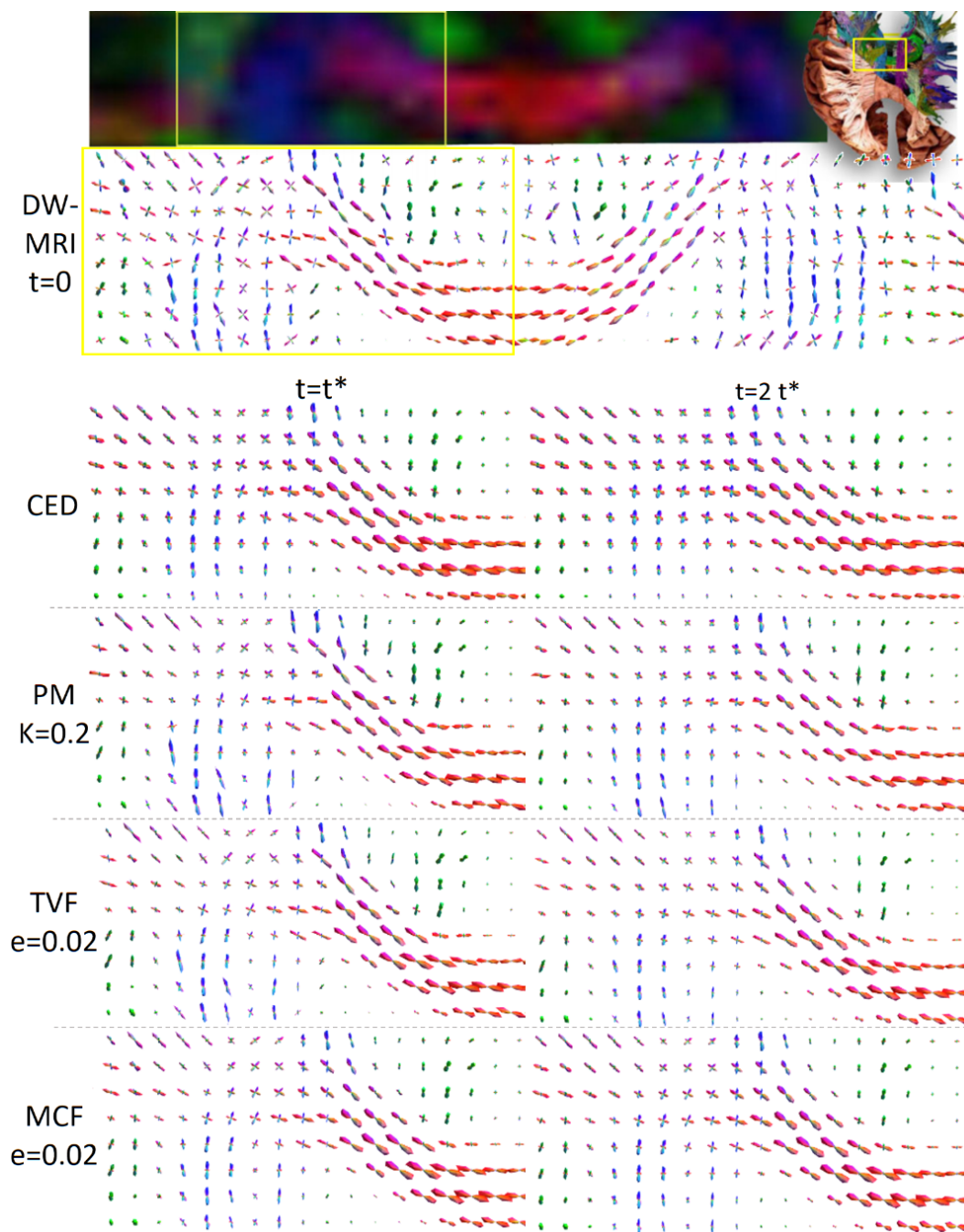


Fig. 16: Qualitative comparison of denoising a FODF obtained by (CSD) [37] from a standard DW-MRI dataset (with $b = 1000s/mm^2$ and 54 gradient directions). For the CSD we used up to 8th order spherical harmonics, and the FODF is then spherically sampled on a tessellation of the icosahedron with 162 orientations.